



**HAL**  
open science

## Reflectance study of ice and Mars soil simulant associations-II. CO<sub>2</sub> and H<sub>2</sub>O ice

Zuriñe Yoldi, Antoine Pommerol, Olivier Poch, Nicolas Thomas

### ► To cite this version:

Zuriñe Yoldi, Antoine Pommerol, Olivier Poch, Nicolas Thomas. Reflectance study of ice and Mars soil simulant associations-II. CO<sub>2</sub> and H<sub>2</sub>O ice. *Icarus*, 2022, 386, pp.115116. 10.1016/j.icarus.2022.115116 . hal-03852901

**HAL Id: hal-03852901**

**<https://hal.science/hal-03852901>**

Submitted on 15 Nov 2022

**HAL** is a multi-disciplinary open access archive for the deposit and dissemination of scientific research documents, whether they are published or not. The documents may come from teaching and research institutions in France or abroad, or from public or private research centers.

L'archive ouverte pluridisciplinaire **HAL**, est destinée au dépôt et à la diffusion de documents scientifiques de niveau recherche, publiés ou non, émanant des établissements d'enseignement et de recherche français ou étrangers, des laboratoires publics ou privés.

## Reflectance study of ice and Mars soil simulant associations – II. CO<sub>2</sub> and H<sub>2</sub>O ice.

Zuriñe Yoldi<sup>1\*</sup>, Antoine Pommerol<sup>1</sup>, Olivier Poch<sup>1,2</sup>, Nicolas Thomas<sup>1</sup>

<sup>1</sup>*Physikalisches Institut, Universität Bern and NCCR PlanetS, Sidlerstrasse 5, 3012  
Bern, Switzerland.*

<sup>2</sup>*Univ. Grenoble Alpes, CNRS, IPAG, 38000 Grenoble, France*

\* *Now at the section for the Physics of Ice, Climate and Earth at the Niels Bohr  
Institute, University of Copenhagen.*

---

### Abstract

We measure the visible and near-infrared reflectance of icy analogues of the Martian surface made of CO<sub>2</sub> ice associated in different ways with H<sub>2</sub>O ice and the regolith simulant JSC Mars-1. Such experimental results obtained with well-controlled samples in the laboratory are precious to interpret quantitatively the imaging and spectral data collected by various Mars orbiters, landers and rovers. Producing and maintaining well-characterized icy samples while acquiring dense spectro-photometric measurements is however challenging and we discuss some of the difficulties encountered in preparing and measuring our samples. We present the results in the form of photometric and spectral criteria computed from the spectra and plotted as a function of the composition and physical properties of the samples. Consistent with previous studies, we find that when intimately mixed with other materials, including water ice, CO<sub>2</sub> ice becomes rapidly undetectable due to its low absorptivity. As low as 5 wt.% of fine-grained H<sub>2</sub>O ice is enough to mask entirely the signatures of CO<sub>2</sub>. Similarly, sublimation experiments performed

with ternary mixtures of CO<sub>2</sub> ice, H<sub>2</sub>O ice and JSC Mars-1 show that water, even when present as a minor component (3 wt.%), determines the texture and evolution of the mixtures. We assess the ability of various combinations of spectral parameters to identify samples with H<sub>2</sub>O, CO<sub>2</sub>, JSC Mars-1, or various mixtures from their reflectance and orient our study to helping interpret ice and soil reflectance spectra from the Martian surface. From the laboratory spectra, we simulate the colour signal generated by the CaSSIS instrument to allow for direct comparisons with results from this instrument and provide to databases the necessary spectral data to perform the same operations with other instruments.

*Keywords:* Reflectance, CO<sub>2</sub> ice, Mixture, Mars, H<sub>2</sub>O ice, Polar Caps

---

# 1. Introduction

## 1.1. *CO<sub>2</sub> ice and the martian CO<sub>2</sub> cycle*

Solid carbon dioxide (CO<sub>2</sub> ice) is present at the surface of various bodies of the Solar System, such as comet 67P-CG [1], Triton [2] or Mars. In the case of Mars, where it represents 96% of the atmosphere [3], CO<sub>2</sub> drives the condensation flow [4]: as a result of the current obliquity of Mars ( $\sim 25^\circ$ ), its hemispheres do not receive the same amount of sunlight, which results in seasonal differences of temperature and pressure conditions in each hemisphere. As a consequence, a large fraction of the atmosphere moves seasonally from the summer hemisphere to the winter hemisphere and back. Almost a quarter of the atmosphere condenses in winter [5], sublimates during spring and migrates to the other hemisphere, where it condenses again to continue the cycle. Beside the CO<sub>2</sub> cycle [6], H<sub>2</sub>O [7] and dust [8] cycles happen yearly within the Martian atmosphere. CO<sub>2</sub> frost has also been detected at all latitudes on Mars [9].

In 1971, Neugebauer et al. [10] confirmed with Mariner 6 and 7 data the predictions previously made by Leighton and Murray [11]: the southern seasonal cap was made of CO<sub>2</sub>. Since then, the community has grown a broad knowledge of the CO<sub>2</sub> and H<sub>2</sub>O condensation/sublimation processes by monitoring the high-latitude regions of Mars with multiple techniques (e.g., gravimetry, gamma-ray and neutron spectrometer, laser altimetry, reflectance spectroscopy or temperature measurements). We know that at the martian mid-to-high latitudes, water ice starts condensing as autumn arrives, first as night-time frost and later as seasonal frost. Once in autumn, the condensation temperature of CO<sub>2</sub> is attained at the surface ( $\sim 150\text{K}$  at

26 6 mbar), causing CO<sub>2</sub> to directly condense on the regolith, or in the atmo-  
27 sphere, causing solidified CO<sub>2</sub> to deposit as frost. In the latter case, CO<sub>2</sub>  
28 can nucleate around atmospheric particles of water ice or dust, resulting in  
29 the cleaning of the atmosphere and contaminated CO<sub>2</sub> ice at the surface.  
30 As spring starts, the first light from the Sun causes the seasonal deposits  
31 to sublimate, first the CO<sub>2</sub> and then H<sub>2</sub>O. By mid-summer, all the seasonal  
32 deposits have sublimated.

### 33 *1.2. Parameters controlling the reflectance - Models*

34 Comparisons of the optical constants of H<sub>2</sub>O and CO<sub>2</sub> ice [12, 13, 14, 15]  
35 already suggest that their spectro-photometric properties will be relatively  
36 similar with very low absorption in the visible spectral range and intense  
37 and wide absorption bands in the near- to mid-infrared. Different types of  
38 radiative transfer models and numerical simulations [16, 17, 18, 19, 20] can  
39 then be used to compute the reflectance of a parameterized surface made of  
40 the ices, pure or mixed with contaminants, from their optical constants. The  
41 relevant parameters are related to both the individual grains (size, shape,  
42 surface texture, internal defects and inclusions...) and the macroscopic prop-  
43 erties of the surface (density, roughness...). Because of the similarity of their  
44 optical properties, a lot of what is known about water ice can be extrapo-  
45 lated to carbon dioxide ice while one should always keep an eye on the known  
46 differences.

47 The physical size of the ice articles plays a very large role in the re-  
48 flectance of icy surfaces. In the visible spectral range, fine grained ( $\lesssim 100$   
49  $\mu\text{m}$ ) frost and snow made of both CO<sub>2</sub> and H<sub>2</sub>O in their pure form present  
50 a very high reflectance and thin ( $\lesssim 1$  cm) layers are sufficient to hide the

51 substrate and reflect nearly 100% of the incident light. The bidirectional  
52 reflectance behaviour of water snow is also observed to be nearly lambertian,  
53 i.e. the measured radiance does not depend on the position of the observer  
54 and shows a cosine dependence on the light incidence angle. Coarse grained  
55 and compact ice however can transmit the light to large depth and the ef-  
56 fects of absorption can be observed because of the long optical path. This  
57 gives rise for instance to the blue colour of the compact ice in glaciers as the  
58 absorption index of H<sub>2</sub>O increases with wavelength. In the near- and mid-  
59 infrared spectra of both H<sub>2</sub>O and CO<sub>2</sub>, the depths of the absorption bands  
60 are strongly influenced by particle size and the most intense bands quickly  
61 saturate for coarse grained and compact ice. Note that CO<sub>2</sub> displays sharper  
62 and less intense infrared absorption bands than H<sub>2</sub>O overall resulting in a  
63 significantly higher albedo for a given particle size [19].

64 Beside particle size, the other parameter which strongly influences the  
65 reflectance of icy surfaces is the presence of contaminants, even in trace  
66 amount and the way they are aggregated with the ice (intimate or geographic  
67 mixtures, coating at the surface of the grains...). It has already been shown in  
68 a variety of contexts that tiny amounts of dark contaminants are sufficient to  
69 hide the photometric signatures of water ice. For instance, Yoldi et al. [21]  
70 show experimentally that intimate mixtures of fine grained basalt powder  
71 and coarser grained water ice do not appear brighter than the pure basalt  
72 powder even with three times more ice than basalt in the mixture. Khuller  
73 et al. [20] model binary mixtures of water ice and Martian dust and find that  
74 less than 1 % of dust mixed with fine grained ice can reduce its albedo by a  
75 factor of 10.

76 *1.3. Observations of CO<sub>2</sub> ice in the southern hemisphere*

77 In the southern Martian hemisphere, a small and thin (< 20 m) perma-  
78 nent cap of CO<sub>2</sub> ice [22] covers part of a much larger km-thick unit known  
79 as the South Polar Layered Deposits (SPLD). This unit is made essentially  
80 of water ice mixed with dust [23, 24] but some ancient and massive deposits  
81 of carbon dioxide ice have also been found [25]. The water ice is exposed  
82 at a few places, notably along scarps [23, 26] but is otherwise covered by a  
83 desiccated dust layer.

84 In winter, seasonal ice deposits extend well beyond the limits of the SPLD  
85 to reach a latitude of about 50 degrees and recede during spring until only  
86 the permanent CO<sub>2</sub> cap is left in Summer. Calvin and Martin [27] and later  
87 on Kieffer et al. [28] studied the evolution of the southern seasonal cap to  
88 discover that it was controlled by CO<sub>2</sub> grain size. They found both long and  
89 short optical path lengths, compatible with ice slabs (metres) and smaller  
90 (centimetres) grains of CO<sub>2</sub> ice, respectively. The size of the CO<sub>2</sub> ice grains is  
91 the primary cause for albedo variations. The presence of translucent slab ice  
92 in the so-called cryptic region at the beginning of spring is also hypothesised  
93 to be the reason for the intense jet activity observed and attributed to solid  
94 state greenhouse effect within the layer of translucent CO<sub>2</sub> ice [29].

95 Langevin et al. [30] used the Observatoire pour la Minéralogie, l'Eau, les  
96 Glaces, et l'Activité (OMEGA) on Mars Express to monitor the evolution of  
97 the southern seasonal cap from the southern winter solstice to mid-summer.  
98 The observations were consistent with the presence of transparent CO<sub>2</sub> slabs  
99 but also locally with events related to the sublimation and re-condensation  
100 of water ice. With the Compact Reconnaissance Imaging Spectrometer for

101 Mars (CRISM, Murchie et al. [31]) and the Mars Color Imager (MARCI, Bell  
102 et al. [32]), on Mars Reconnaissance Orbiter, Brown et al. [33] confirmed the  
103 presence of pure water ice deposits during the final stages of the recession of  
104 the southern seasonal cap. They also inferred CO<sub>2</sub> grain sizes of up to 70 ±  
105 10 mm before the springtime sublimation of the cap, and of 2.5-5 ± 1 mm  
106 in the residual cap. Using CRISM and the High Resolution Imaging Science  
107 Experiment (HiRISE, McEwen et al. [34]), Pommerol et al. [35] monitored the  
108 evolution of the south polar layered deposits from spring to summer. Around  
109  $L_s \sim 250$  degrees, shortly before the southern summer, they observe an  
110 increase of both the albedo and the strength of the CO<sub>2</sub> ice bond strength,  
111 which they attribute to a cleaning of the icy deposits as they sublimate.

112 Brown et al. [36] studied, with CRISM, the origin of the water ice signa-  
113 ture that had been repeatedly noticed at the southern cap during summer.  
114 They linked this signature with the deposition of atmospheric H<sub>2</sub>O ice on  
115 the cap. They assessed this deposition to an equivalent H<sub>2</sub>O layer of 0.2 mm  
116 and 70% porosity (0.013 g/cm<sup>2</sup>).

#### 117 *1.4. Observations of CO<sub>2</sub> ice in the northern hemisphere*

118 Contrary to the southern hemisphere where the SPLD are almost en-  
119 tirely buried below an optically thick layer of dust and the small CO<sub>2</sub> cap,  
120 the Northern Polar layered Deposits (NPLD) expose a vast surface of water  
121 ice to the atmosphere. This has important consequences for seasonal evo-  
122 lution of northern polar regions. While overall the seasonal processes are  
123 relatively similar in both hemisphere, significant differences exist. In partic-  
124 ular, the seasonal deposits in the northern hemisphere contain much more  
125 water ice than in the southern hemisphere. Using THEMIS [37] and TES

126 [38] data, Wagstaff et al. [39] identified and characterized the seasonal water  
127 ice annulus first hypothesised by [40]. Langevin et al. [41] monitored with  
128 OMEGA the composition of the northern latitudes of Mars. They linked  
129 albedo changes in early summer with an increase in the size of the ice grains.  
130 They also assessed the dust content within the ice to be low (a maximum  
131 of 5% if intimate mixtures and  $\ll 1\%$  if intramixtures). Appéré et al. [42]  
132 used the same instrument to study the retreat of the north seasonal deposits  
133 during two consecutive Martian years, and mapped the temporal and spatial  
134 distributions of CO<sub>2</sub> and H<sub>2</sub>O ice. They observed CO<sub>2</sub> winter condensation  
135 compatible with transparent slabs, surrounded by the water ice annulus. This  
136 annulus consisted first of thin frost and was later covered by water ice grains  
137 that were previously trapped in CO<sub>2</sub>. This surficial water-rich layer dom-  
138 inated the reflectance spectra of the deposits around  $L_S=50^\circ$ , even though  
139 the CO<sub>2</sub> locally reappeared between  $L_S=50^\circ$  and  $L_S=70^\circ$ .

140 Hansen et al. [43], Portyankina et al. [44] and Pommerol et al. [45] studied  
141 dynamic processes in the northern seasonal polar cap by analysing HiRISE  
142 images. Hansen et al. [43] and Portyankina et al. [44] showed that sublima-  
143 tion process play an active role in the erosion of dunes. They conclude that  
144 the same model which explains dynamic southern sublimation processes [29]  
145 is also applicable to fans and dark spots over dunes fields observed in the  
146 northern hemisphere. Pommerol et al. [45] confirmed with CRISM data the  
147 local reappearances of the CO<sub>2</sub> spectral signatures in late spring first seen by  
148 Appéré et al. [42] and hypothesize that the removal of surficial water frost  
149 by local winds explains this evolution.

150 *1.5. Laboratory measurements of CO<sub>2</sub> ice and H<sub>2</sub>O ice mixtures*

151 Numerical models can be used to establish the properties of the polar sur-  
152 faces (see section 1.2). Many experiments have also been conducted on thin  
153 films and single crystals to measure transmission spectra of pure CO<sub>2</sub> ice or  
154 mixtures with H<sub>2</sub>O [46, 47]. However, there is a lack of measured reflectance  
155 data with macroscopic and well-controlled and documented CO<sub>2</sub>-ice samples,  
156 which are needed to calibrate the models and validate the interpretations.  
157 This is explained by the technical challenges that working with large amounts  
158 of CO<sub>2</sub> ice entails: for example, its fast sublimation and the over-pressure  
159 that it might induce if enclosed or its propensity to cold trap water frost from  
160 the atmosphere. We summarise here the most relevant experimental studies  
161 on the reflectance of CO<sub>2</sub> ice.

162 In the late 60s, Kieffer [48, 49] carried out the first laboratory studies  
163 on the spectral reflectance of CO<sub>2</sub> and H<sub>2</sub>O frosts in the near- to mid- in-  
164 frared (0.8 - 3.2  $\mu\text{m}$ ). By introducing gas of controlled composition into a  
165 cold chamber, he condensed the water and carbon dioxide on the walls and  
166 measured their reflectance from 0.8 to 3.2  $\mu\text{m}$ . He observed a masking of the  
167 CO<sub>2</sub> signatures by H<sub>2</sub>O, thus concluding that a CO<sub>2</sub>-free reflectance spec-  
168 trum does not discard the presence of CO<sub>2</sub>. While the resolution and quality  
169 of the data in the (1.7 - 3.0  $\mu\text{m}$ ) range are sufficient for comparison with  
170 orbital data, the spectral resolution in the (0.8 - 1.7)  $\mu\text{m}$  range is very coarse  
171 and does not allow to resolve the fine CO<sub>2</sub> features. The reflectance was not  
172 measured in the visible range, shortward of 0.8  $\mu\text{m}$ . Despite these issues, this  
173 unique dataset remains one of the best sources of information on the spectral  
174 reflectance of CO<sub>2</sub> ice, half a century after its collection.

175 Similar to Kieffer [49], Bernstein et al. [50] mixed carbon dioxide and  
176 water in their gaseous phases and condensed them to grow frost. They ob-  
177 served a possible enhancement of a CO<sub>2</sub> feature at 2.135 μm in mixtures of  
178 CO<sub>2</sub> with other materials, which they pointed out as a potential indicator of  
179 the presence of CO<sub>2</sub> in mixtures. In the absence of pictures, it is understood  
180 that the samples assessed in their study are thin layers of ice.

181 Oancea et al. [51] measured infrared reflectance spectra of mixtures be-  
182 tween CO<sub>2</sub> and H<sub>2</sub>O to study specifically the spectroscopic signal of CO<sub>2</sub>  
183 clathrate hydrates. They identified two bands of the clathrate at 2.71 and  
184 4.28 μm which can be used for the identifications of such clathrates in remote-  
185 sensing data.

186 The team from IPAG (Institut de Planétologie et d'Astrophysique de  
187 Grenoble) has also presented reflectance measurements of different mixtures  
188 of CO<sub>2</sub> and H<sub>2</sub>O ices. Grisolle et al. [52] condensed various thicknesses of  
189 water frost on a sample of CO<sub>2</sub> snow and studied its reflectance between  
190 1.3-1.7 μm. Philippe et al. [53] and Schmitt et al. [54] have performed sub-  
191 limation experiments with polycrystalline translucent CO<sub>2</sub> ice and dust and  
192 have shown that dust sinking and slab cracking only produce a slight increase  
193 of the continuum reflectance (by 7 %) and a slight decrease of the CO<sub>2</sub> sig-  
194 natures. They find however that compact polycrystalline CO<sub>2</sub> ice becomes  
195 brighter as it sublimates, probably as a result of surface scattering at the  
196 ice/gas interfaces of the joints boundaries as the ice becomes more porous.  
197 This mechanism is hypothesised to explain the brightening of the Martian  
198 seasonal polar caps observed in late Spring.

199 Finally, Portyankina et al. [55] simulated atmospheric conditions of pres-

200 sure and temperature close to the Martian ones and condensed atmospheric  
201 CO<sub>2</sub> on both metallic and dusty surfaces. They assessed the way in which  
202 the CO<sub>2</sub> condensed (e.g. flakes or slab), and confirmed the possibility of CO<sub>2</sub>  
203 to form centimeters-thick, highly translucent slabs of ice depending on the  
204 conditions of temperature and pressure.

### 205 *1.6. Need for additional reflectance measurements*

206 While the spectra published more than 50 years ago by Kieffer [48, 49]  
207 are of excellent quality and with sufficient spectral resolution at wavelengths  
208 larger than 1.6  $\mu\text{m}$ , the shorter wavelength near-infrared is only covered with  
209 a few spectral bands and the visible range was not measured. The spectra  
210 were also normalised to 1, providing no information of the absolute reflectance  
211 level. The first objective of this work is to extend the spectral range for  
212 similar samples over the entire visible (0.4-1.0  $\mu\text{m}$ ) and near-infrared (1-  
213 2.5  $\mu\text{m}$ ) spectral ranges with high signal to noise and spectral resolution  
214 and sampling. Another main objective is to broaden the variety of solid  
215 CO<sub>2</sub> samples available for reflectance studies. In addition to CO<sub>2</sub> slabs, we  
216 introduce ways of producing granulated CO<sub>2</sub> ice samples, which are key to  
217 address the range of grain sizes observed on the Martian surface. We present  
218 a study of the reflectance of CO<sub>2</sub> ice, both pure and intimately mixed with  
219 water ice or JSC Mars-1. We also produced ternary mixtures of CO<sub>2</sub> ice, H<sub>2</sub>O  
220 ice and JSC Mars-1, and monitored their reflectance as the ices sublimated.

221 Our range of analogues necessarily includes idealised and simplified as-  
222 sociations of ices and dust such as homogeneous intimate mixtures of the  
223 CO<sub>2</sub>/H<sub>2</sub>O ices and dust. It is unlikely that any process on Mars will pro-  
224 duce –at a large scale– very homogeneous mixtures but such well-controlled

225 samples are ideal playgrounds for testing reflectance models. More complex  
226 samples are useful too and allow for more direct comparisons with the remote-  
227 sensing data but parameters are more difficult to control and the comparison  
228 with models is more challenging.

229 We discuss lessons learnt and remaining challenges to produce these sam-  
230 ples. We then study strategic spectral criteria to characterise the results of  
231 our experiments, and propose methods to fully exploit our reflectance spec-  
232 tra. The spectra are also available in public databases for further/different  
233 analyses by interested readers. This paper is the continuation of the work  
234 published in Yoldi et al. [56], which provided laboratory data and spectral  
235 analysis to help interpret water ice and soil reflectance spectra from the  
236 Martian surface. Toward the end of the Result and Discussion Sections,  
237 we consider all results from the two articles to provide insights to interpret  
238 remote-sensing colour and spectral information in terms of the composition  
239 and physical properties of Martian icy surfaces.

240 **2. Samples, instruments and methods**

241 *2.1. Samples*

242 *2.1.1. Ices*

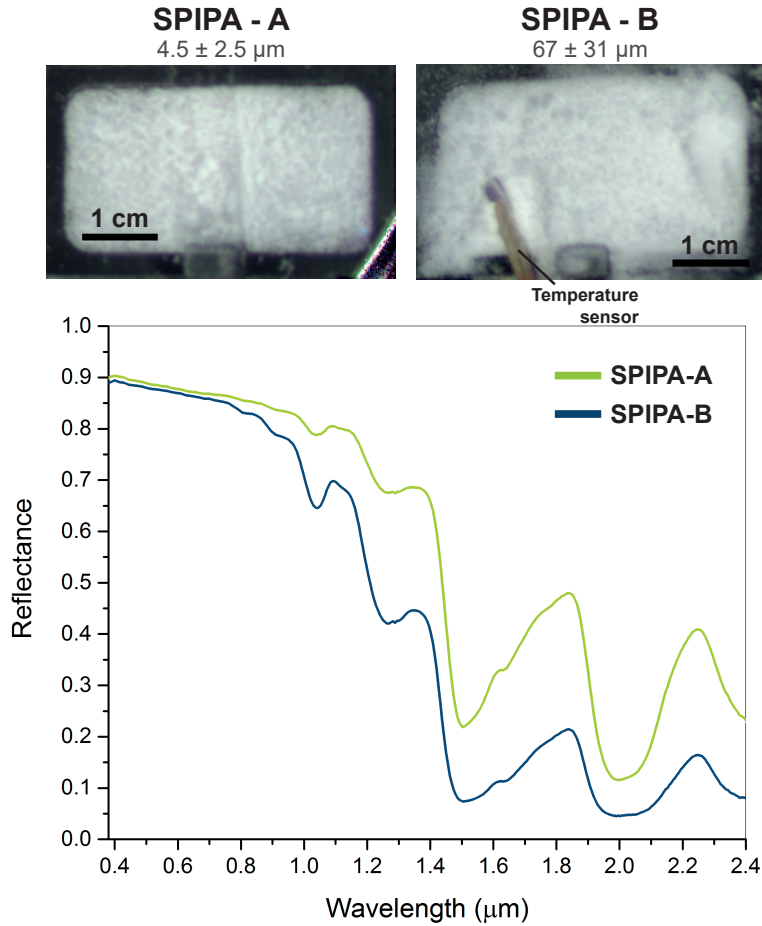


Figure 1: Top: Samples of fine-grained ( $4.5 \mu\text{m}$ , SPIPA-A)  $\text{H}_2\text{O}$  (left) and coarser grained ( $67 \mu\text{m}$ , SPIPA-B)  $\text{H}_2\text{O}$  (right) ices. Bottom: reflectance spectra of these two types of water ice.

243  $\text{H}_2\text{O}$  ice. We produced the granular water ice used in this study with the  
244 Setup for Production of Icy Planetary Analogues (SPIPA), at LOSSy. In  
245 this study, we work with fine-grained ice (mean diameter:  $4.5 \pm 2.5 \mu\text{m}$ ) and

246 coarser-grained ice ( $67\pm 31\ \mu\text{m}$ ), which we refer to as SPIPA-A and SPIPA-B  
247 respectively. Both SPIPA ices were produced by freezing nebulised, deionised  
248 water. We obtained different size distributions by using two different systems  
249 to nebulise the water. A detailed description of the production and charac-  
250 terisation of the SPIPA ices is available in Pommerol et al. [57]. Fig 1 shows  
251 pictures of the SPIPA samples, as well as their reflectance spectra.

252 We also caused atmospheric water to condense onto a slab of  $\text{CO}_2$  ice  
253 by exposing the slab to the atmosphere, outdoors, on a day with 93% of  
254 relative atmospheric humidity. Water frost did not condense homogeneously  
255 on the slab, which allowed us to study the spectra of different water frost  
256 thicknesses.

257 *CO<sub>2</sub> ice.* From frost [58] to thick and transparent slabs [59],  $\text{CO}_2$  ice is found  
258 in a variety of particle sizes on the Martian surface. In this study, we have  
259 used three types of pure  $\text{CO}_2$  ice, which we call  $\text{CO}_2$  frost,  $\text{CO}_2$  slab and  
260 crushed  $\text{CO}_2$  (Fig 2). We detail below the process of production of each one  
261 of these samples.

262  $\text{CO}_2$  frost was formed upon adiabatic cooling from pressurised  $\text{CO}_2$  gas us-  
263 ing a commercial  $\text{CO}_2$  dry ice maker (Bel-Art<sup>TM</sup> SP Scienceware<sup>TM</sup> Frigimat<sup>TM</sup>  
264 Junior Dry Ice Make) and immediately stored in liquid nitrogen. Fig 2c  
265 shows a representative microscope image of the  $\text{CO}_2$  frost, from which we  
266 estimate the diameters of the individual  $\text{CO}_2$  grains to range between about  
267  $10\ \mu\text{m}$  and  $100\ \mu\text{m}$  upon formation. The individual grains show a tendency  
268 to sinter as they form. Smooth necks joining the grains are clearly visible  
269 under the microscope, which results in agglomerates of a few hundreds of mi-  
270 crometres. Unfortunately, the rapid sublimation of such fine grains of  $\text{CO}_2$

271 at atmospheric pressure hampered further characterisation of these samples.

272 We have also used commercial CO<sub>2</sub> ice pellets purchased from Carbagas  
273 AG (1.4 kg slices, Reference: I5891XXX) and delivered in wedge-shaped  
274 ingots of few centimetres of maximal thickness. The ice is compact and  
275 translucent but not transparent. Internal fractures and joints are visible and  
276 scatter the light internally (2a). Note that the bare black rims of the sample  
277 holder cannot be distinguished from the frost-covered white surface through  
278 the cm-thick slab ice. We refer to these pellets as slab CO<sub>2</sub> ice hereafter.  
279 We broke the slabs into small pieces to place them in the sample holder, as  
280 can be seen in Figure 2a. We crushed some of the slabs and dry-sieved the  
281 resulting powder to obtain samples of CO<sub>2</sub> ice with various size distributions.  
282 We prepared three size distributions (Fig 2a): particles between 400 and 800  
283  $\mu\text{m}$ , particles between 200 and 400  $\mu\text{m}$  and particles smaller than 200  $\mu\text{m}$ . Fig  
284 2b shows an optical microscope picture of the fraction between 400 and 800  
285  $\mu\text{m}$ . Unlike CO<sub>2</sub> frost, the crushed particles appear angular to sub-rounded  
286 because of the crushing process. Note also the fine-scale surface texture and  
287 the presence of internal fractures, pores or other types of defects within some  
288 of the particles (lower right corner) which effectively scatter the light

### 289 *2.1.2. Martian analogues*

290 As a Martian soil analogue, we have used the Martian regolith simulant  
291 JSC Mars-1 [61], distributed by the Johnson Space Center. We already used  
292 this simulant in the first paper of this series [56].

293 For part of this study, we have used the JSC Mars-1 as distributed; all  
294 the specifications regarding particle sizes, density, etc. are provided in Allen  
295 et al. [61]. We have also dry-sieved some of the original JSC Mars-1 to

296 retrieve grains smaller than 100  $\mu\text{m}$ , which we used for the ternary mixtures.  
297 A Scanning Electron Microscope (SEM) picture of the fine grains and the  
298 reflectance spectra of both the original and the fine distributions are shown  
299 in Fig 3. Note that the size of the the fine Martian aeolian dust is estimated  
300 to be  $\sim 2 \mu\text{m}$  [62, 63] and while our fine fraction contains such very fine  
301 particles in large number, its mass distribution is dominated by the largest  
302 ones. In some contexts however, a broader size distribution is preferable.  
303 For instance, the jet activity observed over the cryptic region in the southern  
304 hemisphere and over dune fields in both hemispheres is known to mobilize  
305 and erode the Martian soil, depositing particles of all sizes over the seasonal  
306 ice.

### 307 *2.1.3. Mixtures*

308 Here, we explain the methodology followed to create the mixtures used in  
309 this study. Table 1 provides an overview of the parameters and specifications  
310 of the samples.

311 *Binary mixtures.* We have developed and validated protocols to create in-  
312 timate mixtures of water ice and refractory materials [57]. These protocols  
313 standardise the mixture production to guarantee the homogeneity and repro-  
314 ducibility of the samples. In short, we blend the ice and refractory materials  
315 with the help of a vortex shaker, alternating shaking and cooling intervals,  
316 during which we plunge the container with the samples into  $\text{LN}_2$ . The dura-  
317 tion of these intervals is stipulated in the protocols.

318 We have adapted those protocols to produce  $\text{CO}_2$  icy samples. The main  
319 difficulty of the process is the different sublimation points of  $\text{H}_2\text{O}$  (273 K) and

320 CO<sub>2</sub> (195 K) at 1 atm. To keep our working temperatures to a minimum, we  
321 kept the samples in aluminium bottles, which we plunged in LN<sub>2</sub>. We took  
322 the bottles out of the nitrogen to weigh and mix the materials in intervals  
323 of maximum 15 seconds. We also kept the sample holders (2x4x2 cm) into  
324 LN<sub>2</sub> until filled with the samples, and the cylinder that contained the sample  
325 holder was filled with LN<sub>2</sub>, as previously explained. The sample holders were  
326 filled inside a freezer to prevent water frost deposition.

327 We prepared the following intimate mixtures:

328 1. CO<sub>2</sub>-H<sub>2</sub>O: we mixed both crushed CO<sub>2</sub> and CO<sub>2</sub> frost with both fine  
329 grained and coarser grained H<sub>2</sub>O ice. We worked with small water  
330 weight percentages (10, 5 and 3 wt%) since it has already been shown  
331 that the water signature dominates the reflectance spectra from small  
332 quantities [49, 19]. Fig 4a shows intimate mixtures of CO<sub>2</sub> frost (10-  
333 100 μm) and fine grained H<sub>2</sub>O ice (~ 4 μm). Fig 4b shows intimate  
334 mixtures of crushed CO<sub>2</sub> and coarser grained H<sub>2</sub>O ice.

335 2. CO<sub>2</sub>-JSC Mars-1 intimate mixtures: by partitioning the sample holder,  
336 we obtained small volumes (2x2x2 cm) for multiple samples (Fig 4d).  
337 This way, we managed to measure several samples under the same  
338 conditions. JSC Mars-1 was mixed with 75, 50, 35, 10 and 5 wt% of  
339 crushed-CO<sub>2</sub>.

340 Even though the materials were homogeneously mixed, the reproducibil-  
341 ity of the intimate mixtures of H<sub>2</sub>O and CO<sub>2</sub> can be improved. For example,  
342 we observed the formation of pebble-like agglomerates for distinct grain sizes

343 and water ice contents. Mixing materials in such ratios is challenging; the  
344 accuracy of water ice concentrations lower than 5 wt% is limited.

345 We also cannot exclude vertical variability within our samples. Either  
346 because of vertical segregation of particle sizes as we fill the holders with the  
347 particulate samples or as a result of thermo-physical evolutions of the sam-  
348 ples (through sublimation, sintering...). Unfortunately, we have no means of  
349 assessing if vertical gradients of samples properties exist and their amplitude.

350 *Ternary mixtures.* We have developed a new methodology to create homoge-  
351 neous mixtures of dust, CO<sub>2</sub> frost and H<sub>2</sub>O ice. These ternary mixtures will  
352 eventually be useful to simulate the volatile sublimation sequence observed  
353 during the retreat of the northern seasonal polar cap of Mars [30, 42, 45]. For  
354 these mixtures, we used the fine fraction of JSC Mars-1 (<100 μm) to sim-  
355 ulate the dust grains suspended in the atmosphere that get trapped within  
356 the ice as CO<sub>2</sub> and H<sub>2</sub>O condense.

357 Figure 5 illustrates the process of production of the ternary mixtures.  
358 First, we produce the CO<sub>2</sub> frost, weigh it and immediately plunge it into  
359 LN<sub>2</sub>. We produce the H<sub>2</sub>O ice, and add it to the LN<sub>2</sub> and CO<sub>2</sub> mixture. We  
360 then add the dust to the mixture. At this point, the mixture looks as shown  
361 in Fig 5a. Table 1 shows the mass percentages used in each case.

362 When the LN<sub>2</sub> has evaporated enough that the liquid surface is below the  
363 top of the powder, the mixture presents a texture similar to that of plaster.  
364 We stir softly but constantly to mix the components of the mixture while the  
365 remaining nitrogen evaporates. Once the LN<sub>2</sub> has evaporated entirely, the  
366 mix solidifies (Fig 5b). Visual inspection confirms that the dust grains are  
367 homogeneously distributed within the ice. Further stirring resulted in the

368 loosening of the sample, whereas the non-manipulated sample would tend to  
369 compact as the CO<sub>2</sub> particles -in our case, the main component- sintered.

370 We present two different textures of the ternary mixtures: a powder-like  
371 one and a compressed one. The density of the samples was  $\rho_{fineH_2O} = 0.47 \text{ g/cm}^3$   
372 and  $\rho_{coarserH_2O} = 0.488 \text{ g/cm}^3$  for the powdered samples and  $\rho_{fineH_2O} = 0.89 \text{ g/cm}^3$   
373 and  $\rho_{coarserH_2O} = 0.846 \text{ g/cm}^3$  for the compacted ones. Fig 6a shows a mi-  
374 croscope image of the powdered ternary mixture (with SPIPA-B). Seconds  
375 later, as CO<sub>2</sub> ice sublimated, the water particles became visible, as can be  
376 seen marked with red arrows in Fig 6b. Finally, Fig 6c shows the ternary  
377 mixture with SPIPA-B spread on a table; the sample on the left was spread  
378 on the table few minutes before the acquisition of the picture, and the sam-  
379 ple on the right was spread right before acquiring the image. On the left,  
380 the carbon dioxide had completely sublimated, and only water ice and JSC  
381 Mars-1 is left.

382 Even though this protocol was effective to produce mixtures with both  
383 fine and coarser-grained H<sub>2</sub>O ice, we observed differences when using one  
384 or the other type of water ice. For example, the grains of the fine-grained  
385 water ice floated in liquid nitrogen forming aggregates, probably increasing  
386 the effective scatterer size of the water ice if they were not destroyed before  
387 solidification.

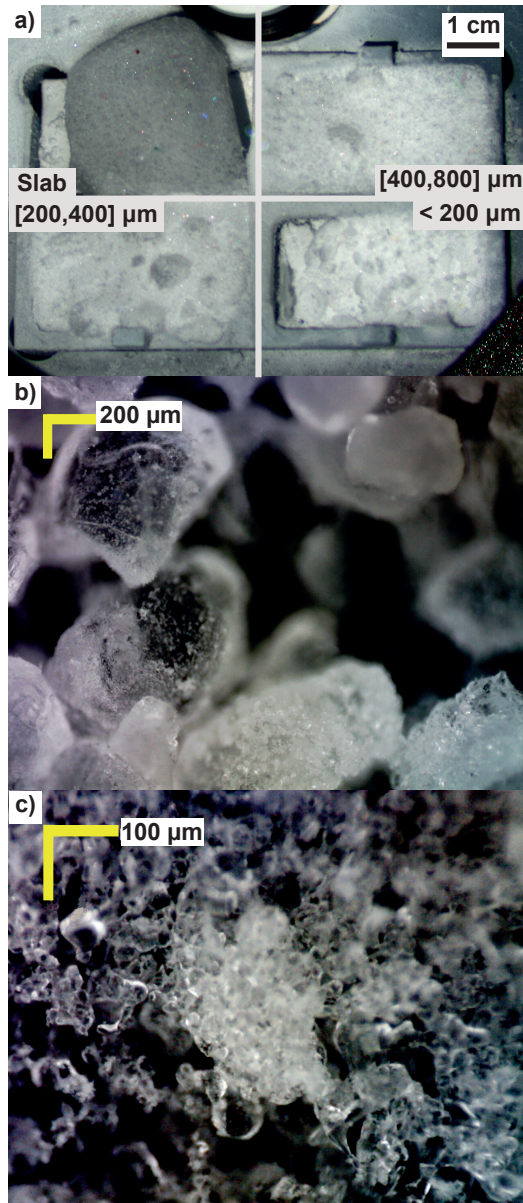


Figure 2: a) Three size fractions of crushed  $\text{CO}_2$  ( $400\text{-}800\ \mu\text{m}$ ,  $200\text{-}400\ \mu\text{m}$  and  $< 200\ \mu\text{m}$ ), along with a  $\text{CO}_2$  slab. These RGB images are exported from the hyperspectral cubes and appear slightly blurry due to the wide spectral range of the measurement. The resolution is  $\sim 50\ \mu\text{m}$ . b) Microscope image of the crushed  $\text{CO}_2$  ( $400\text{-}800\ \mu\text{m}$  fraction). c) Microscope image of the  $\text{CO}_2$  frost showing smooth and roundish particles with diameters ranging between  $10$  and  $100\ \mu\text{m}$ . Many of the particles show clear signs of sintering, being connected by small necks.

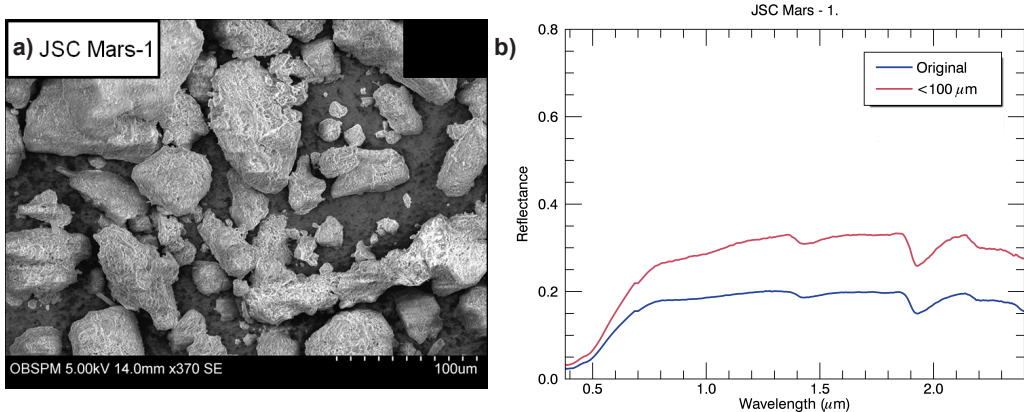


Figure 3: a) SEM picture of a sieved sample of JSC Mars-1 (<80 μm). Picture extracted from Brouet [60]. b) Reflectance spectra of the original and sieved fraction (<100 μm) of the JSC Mars-1

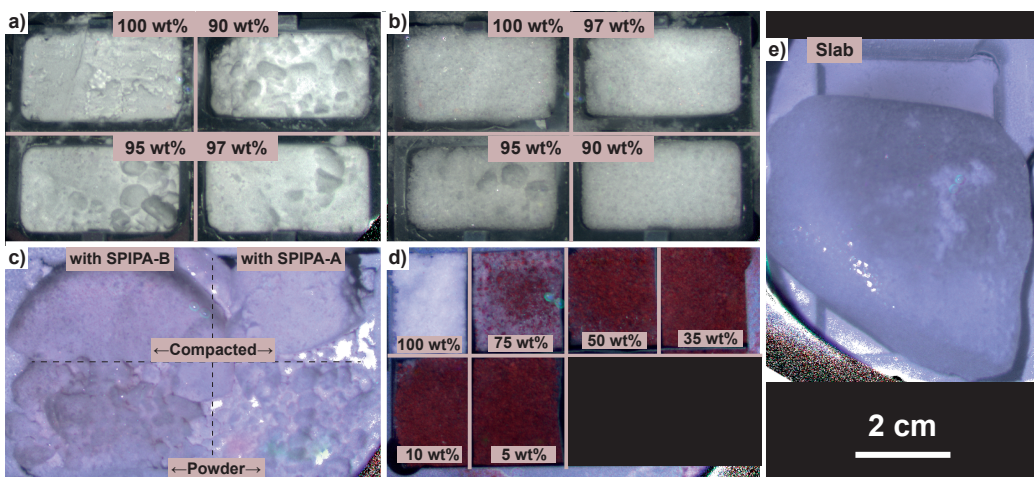


Figure 4: Mixtures with CO<sub>2</sub> ice. a) Various weight percentages of CO<sub>2</sub> frost (10-100 μm) intimately mixed with fine grained (~ 4.5 μm) water ice. b) Various weight percentages of crushed CO<sub>2</sub> (400-800 μm) intimately mixed with coarser grained (~ 67 μm) water ice. c) Ternary mixtures of CO<sub>2</sub>, fine grained H<sub>2</sub>O (right) or coarser grained H<sub>2</sub>O (left), and JSC Mars-1. On top, the mixtures have been compacted. d) Various weight percentages of crushed CO<sub>2</sub> (400-800 μm) intimately mixed with JSC Mars-1. e) Slab of compact CO<sub>2</sub> ice with some water frost (white) on the right side.

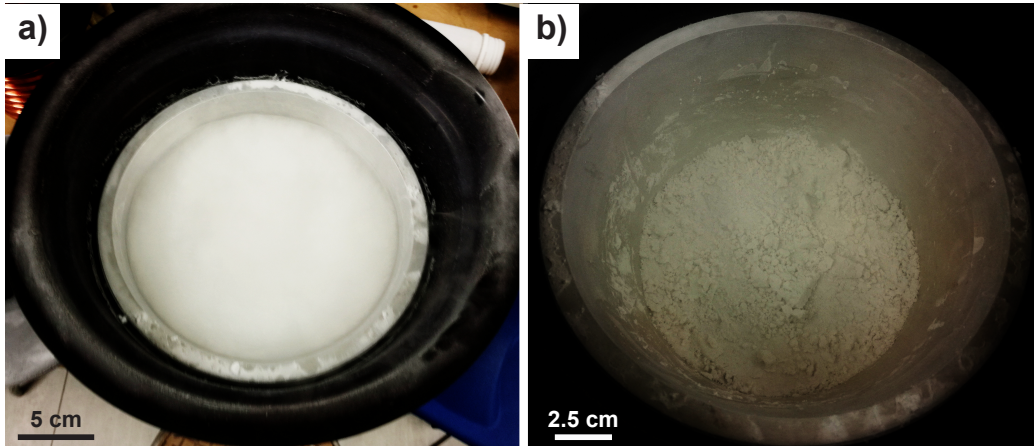


Figure 5: Two steps of the production of ternary mixtures. a)  $\text{CO}_2$  frost (10-100  $\mu\text{m}$ ), coarser grained  $\text{H}_2\text{O}$  ice ( $\sim 60 \mu\text{m}$ ) and JSC Mars-1 in liquid nitrogen. b) After sublimation of the liquid nitrogen, the components of the mixture settle down.

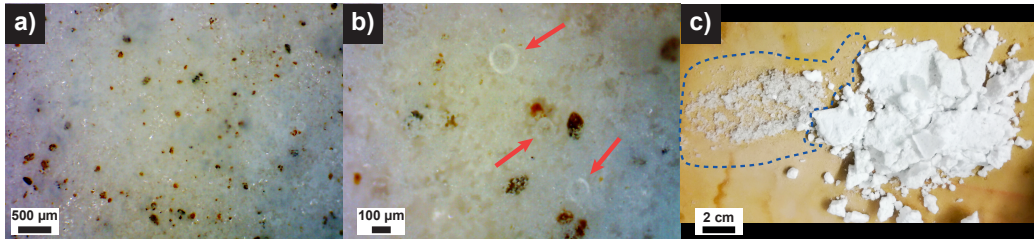


Figure 6: Sublimation of  $\text{CO}_2$  ice in the ternary mixtures. a) Microscope picture from the ternary mixture upon production. b) A few seconds afterwards, the first layer of  $\text{CO}_2$  has sublimated, revealing the SPIPA-B particles in the mixture (marked with red arrows). c) The ternary mixture left on a table for a few minutes (left) and freshly spread (right). The sample on the left has lost all the  $\text{CO}_2$  (whose initial contour is shown with the blue, dashed line), releasing the coarser  $\text{CO}_2$  ice grains and JSC Mars-1.

Mixing Mode	CO <sub>2</sub>	Size of CO <sub>2</sub> ice	Contaminant	Size of the Contaminant	Concentration of contaminant	T <sub>Shroud</sub> (K)	Duration of Measurements
—	Crushed	400-800 $\mu\text{m}$	—	—	—	128 K	1st scan: 30 mins Hyperspectral: 71 mins
Frost	Slab	Wedge shaped. Max dim: 8 x 5 x 2.8 cm	Water frost	Unknown.	From $\mu\text{m}$ to ~mm-thick layer	160 K	1st scan: 30 mins Hyperspectral: 71 mins
Intimate mixture	Frost	Few $\mu\text{m}$ . Agglomerates of hundreds of $\mu\text{m}$	SPIPA-A	4.5 $\pm$ 2.5 $\mu\text{m}$	148 K	138 K	1st scan: 30 mins Hyperspectral: 71 mins
			SPIPA-B	69 $\pm$ 31 $\mu\text{m}$	3, 5, 10 wt%		
	Crushed	400-800 $\mu\text{m}$	SPIPA-A	4.5 $\pm$ 2.5 $\mu\text{m}$	140 K	150 K	
			SPIPA-B	69 $\pm$ 31 $\mu\text{m}$			
Ternary Intimate mixture	Frost	Few $\mu\text{m}$ . Agglomerates of hundreds of $\mu\text{m}$	JSC Mars-1	71.7% > 150 $\mu\text{m}$ 28.3% < 150 $\mu\text{m}$ [61]	25, 50, 65, 90, 95 wt%	160 K	Total time: 11scans * 32 mins
			SPIPA-A	4.5 $\pm$ 2.5 $\mu\text{m}$	3 wt%	See Fig 7	
			JSC Mars-1	<100 $\mu\text{m}$	0.2 wt%		
			SPIPA-B	69 $\pm$ 31 $\mu\text{m}$	3 wt%		
JSC Mars-1	<100 $\mu\text{m}$	0.2 wt%					

Table 1: Summary of the compositions, concentrations, mixture types and acquisition conditions of the experiments reported in this study.

388 *2.2. Instrument description*

389 We have acquired the reflectance data presented in this study with the  
390 Simulation Chamber for Imaging Temporal Evolution of Analogous Samples  
391 (SCITEAS) at LOSSy, the Laboratory for Outflow Studies of Sublimating  
392 icy materials of the University of Bern. SCITEAS is a vacuum and cold  
393 chamber monitored with an imaging system that allows us to characterise  
394 ice-bearing samples. Pommerol et al. [64] first described SCITEAS in 2015.  
395 In the first paper of this series [56], we have detailed improvements to the  
396 system. Further details, together with a list of the published studies carried  
397 out with SCITEAS can be found in Pommerol et al. [57]. Therefore, we only  
398 provide here the main characteristics of the instrument:

- 399 • Acquisition of hyper/multispectral cubes between 0.38 and 2.5  $\mu\text{m}$ .
- 400 • Samples can be kept at low temperature (down to 100 K) by flowing  
401 liquid nitrogen ( $\text{LN}_2$ ) through a cold shroud that surrounds the sample  
402 holder.
- 403 • The pressure can be reduced down to  $10^{-6}$  mbar.
- 404 • The spectral sampling is defined by the user. For hyperspectral acqui-  
405 sitions, we typically work with a sampling of 15 nm in the visible (VIS,  
406 0.4-0.95  $\mu\text{m}$ ) and of 6 nm in the near-infrared (NIR, 0.95- 2.500  $\mu\text{m}$ ).
- 407 • The geometrical configuration of the instrument is set by default so  
408 that the incidence angle is around  $20^\circ$ , the emission angle is  $30^\circ$  and  
409 the phase angles are  $50^\circ$  in the visible and  $10^\circ$  in the near-infrared [64].

410 • The samples holder are made of aluminum and covered by a layer of  
411 black aluminum tape which has a constant reflectance of 0.05 over the  
412 entire spectral range investigated here. The holders are rectangular  
413 with LxWxH dimensions of 4x2x2cm.

414 At the time these experiments were conducted, the vacuum pumps of  
415 SCITEAS could not pump the CO<sub>2</sub> out of the chamber at a rate that would  
416 avoid building up pressure inside of it. The chamber was also not equipped  
417 with a cold plate below the sample. Both features were added later as a re-  
418 vised version of the chamber (SCITEAS-2) was built [65]. For safety reasons,  
419 we did not close the lid of the chamber completely when working with CO<sub>2</sub>  
420 ice to let the gas produced by sublimation escape from the chamber.

421 Performing the experiments under the laboratory atmosphere is of course  
422 different from the Martian conditions. There are two aspects to consider:  
423 First, the absolute pressure is higher by a factor of  $\sim 100$  and second the  
424 sublimation of CO<sub>2</sub> in the laboratory takes place in an inert atmosphere of  
425 nitrogen and oxygen with only traces of CO<sub>2</sub> while on Mars there is an equi-  
426 librium between a CO<sub>2</sub> ice surface and a CO<sub>2</sub> atmosphere. As a result of  
427 the absolute difference of pressure, sublimation in the lab will also occur at a  
428 higher temperature (195K vs. 140K), following the ClausiusClapeyron rela-  
429 tion. This will not affect the behaviour of water which is always far below its  
430 sublimation temperature in both cases. Higher pressure can also increase the  
431 vertical heat transport within the sample through gas conduction and con-  
432 vection, which in turn could have consequences for the metamorphism of the  
433 sample at various depths. Sublimating CO<sub>2</sub> ice in an inert gas atmosphere  
434 rather than in equilibrium with its pure gas phase is also likely to change

435 the outcome of the sublimation by affecting the sublimation speed and pos-  
436 sible vertical transport and recondensation of CO<sub>2</sub> within the porosity of the  
437 sample [66]. Future work will ideally attempt to perform these sublimation  
438 experiments in conditions closer to the Martian surface and find out if the  
439 possible differences discussed here are indeed significant. Note that the in-  
440 fluence of lab pressure is not only relevant for the sublimation but also for  
441 the growth. For example, [48] suggest that for a process limited by diffusion,  
442 the size of the frost crystals is proportional to the relative concentration of  
443 the condensible gas. Consequently, we can expect the Martian crystals of  
444 frost to be smaller than the ones grown in the laboratory. The effect of pres-  
445 sure (and temperature) on the morphology of crystals grown was studied  
446 experimentally by Portyankina et al. [55].

#### 447 2.2.1. Acquisition time

448 The acquisition of a hyperspectral cube under the current setting lasts  
449 70 min [56]. However, CO<sub>2</sub> sublimates faster than that at the range of  
450 temperatures and pressures we work with. We have modified that spectral  
451 sampling to reduce the duration of the measurements: even though we keep  
452 the 6 nm sampling around absorption features in the NIR, we measure the  
453 reflectance only at specific wavelengths in the continuum. This acquisition  
454 mode lasts 30 min and will be referred to as *quick scan*.

455 Most of our measurements consist of a first, quick scan followed by a  
456 complete one. The second scan provides us with the entire shape of the  
457 spectra but with a larger CO<sub>2</sub> grain size due to sintering and/or reduced  
458 concentration of the finest grains of CO<sub>2</sub> due to sublimation. To monitor the  
459 sublimation of ices in the ternary mixtures at high temporal resolution, we

460 have used only quick scans.

### 461 *2.2.2. Sublimation of ice from the samples*

462 At a constant pressure (i.e. 1 atm) and for a given grain size, temperature  
463 controls the sublimation of our ices. Table 1 shows the mean temperature  
464 measured on the shroud for each experiment. To reach such low temperatures  
465 at 1 atm, we filled the cylinder containing the sample holder (see Fig 2 in  
466 Pommerol et al. [64]) with LN<sub>2</sub> at the beginning of the experiment.

467 The evolution of temperature measured in the shroud and the air near  
468 the ternary mixtures is shown in Figure 7, where we have also marked the  
469 times at which each measurement (12 in total) started. The steep increase of  
470 temperature observed at t=140 min was intentional to speed up sublimation.

### 471 *2.2.3. Water frost condensation on the samples*

472 As mentioned before, we were not able to seal the cold chamber during  
473 the experiments. However, the constant and intense out-gassing of the LN<sub>2</sub>  
474 from the sample holder keeps the chamber very dry, as nitrogen pushes the  
475 air out of the compartment. This keeps water frost deposition to a minimum,  
476 but does not completely avoid it.

477 To assess the amount of water cold trapped onto our samples, we added  
478 a control sample of pure CO<sub>2</sub> ice in each set of experiments. The H<sub>2</sub>O index  
479 at 1.5 μm (see Section 2.3.2) of the control samples allows us to assess the  
480 water frost trapped by the samples. While we do not have any way to directly  
481 assess the quantity of frost deposited, we can use empirical relations derived  
482 from previous work to estimate the frost thickness from the strength of the  
483 water absorption bands. In our previous work [56], we had used the 2-μm

Temperature evolution in sublimation series.

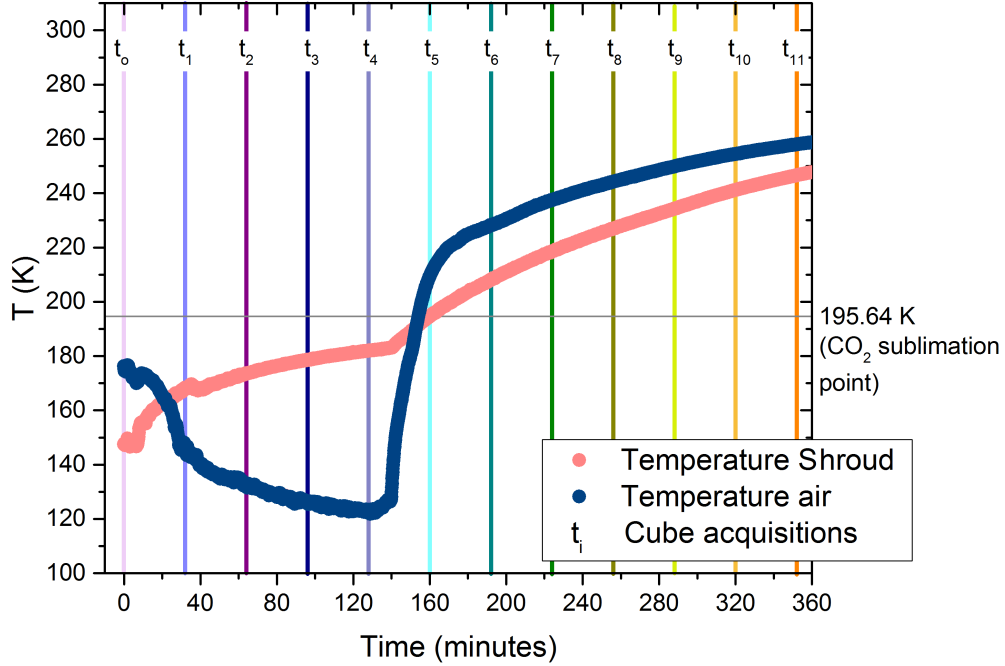


Figure 7: Evolution of the temperature of the shroud and the air at the surface surrounding the samples. The vertical lines indicate the time of acquisition of each of the 12 quick scans performed during the experiment. The horizontal line indicates the sublimation temperature of  $\text{CO}_2$  at atmospheric pressure.

484 band of  $\text{H}_2\text{O}$  for this purpose and an empirical relation derived from the data  
 485 published by Clark and Lucey [67]. Here, we cannot use the 2- $\mu\text{m}$  absorption  
 486 band of water because of the strong overlapping absorption of  $\text{CO}_2$  but the  
 487 1.5- $\mu\text{m}$   $\text{H}_2\text{O}$  band does not suffer from this problem. Digitizing the data from  
 488 Clark and Lucey [67] for water frost grown over a Mauna Kea dust sample, we  
 489 find a logarithmic relationship between the 1.5 $\mu\text{m}$  band depth and the frost  
 490 thickness. Digitizing as well the two spectra from Kieffer [48] for  $\text{H}_2\text{O}$  frost  
 491 grown over  $\text{CO}_2$  (same as in our work) and assuming a typical porosity of 90

492 % [68], we notice that these two points fall over the same trend. This trend  
493 allows us to roughly estimate the frost thicknesses mentioned in the following  
494 sections, which vary between 25 and 400  $\mu\text{m}$  depending on the sample and  
495 the duration of the exposure to moist air. While the consistency between  
496 the results of [48] and Clark and Lucey [67] gives us confidence that these  
497 estimates are credible, an independent way to assess the thickness of the frost  
498 layer would be preferable and new developments are planned to allow such  
499 observations.

### 500 *2.3. Data processing*

501 We convert the raw data into reflectance factor (REFF) units (as defined  
502 by Hapke [18]) through a calibration process detailed in Pommerol et al. [64].  
503 We provide here the main steps of that process:

- 504 1. Before the measurement of the actual samples, we perform similar mea-  
505 surements (same cameras settings, spectral ranges and sampling, sam-  
506 ple position) with a large, nearly-Lambertian surface (Spectralon<sup>TM</sup>  
507 (Labsphere)) covering the field-of-view of the camera.
- 508 2. Regularly during the measurements of the spectral cubes, we close a  
509 shutter installed at the monochromator and acquire dark images with  
510 the exact same settings as the actual images.
- 511 3. We interpolate temporally the dark signal and subtract it from the  
512 corresponding cube.
- 513 4. We divide the dark-signal corrected data acquired from the actual sam-  
514 ple by the dark-signal corrected data acquired with the Spectralon sur-

515 face.

516 The calibration procedure outputs a reflectance hyper/multispectral cube in  
517 which we define Regions of Interest (ROIs) to extract averaged reflectance  
518 spectra from the desired areas.

### 519 *2.3.1. Uncertainties*

520 We detail in the first paper of this series [56], the procedure that we follow  
521 to assess the uncertainties of our measurements. Therefore, we only present  
522 here the major points of the procedure.

- 523 • Our sample holders contain an additional calibration target whose re-  
524 flectance is known (i.e. Spectralon<sup>T</sup>M from Labsphere). By tracking  
525 the variation of its reflectance throughout the measurements, we assess  
526 their precision and accuracy.
- 527 • The average precision on our calibration target is  $\pm 0.3\%$  in the VIS  
528 and  $2\%$  in the NIR. This translates into signal-to-noise ratios (SNRs)  
529 of 333 and 50, respectively.
- 530 • Let us assume the scenario in which the uncertainty in the precision is  
531 entirely due to photon noise. In that case, the uncertainty varies with  
532 the square root of the signal, that is, of the reflectance of the sample.  
533 Following this, the SNR drops to 95 in VIS (relative error of  $1\%$ ) and  
534 16 in NIR (relative error of  $6\%$ ) for a sample with a reflectance of  $10\%$ .
- 535 • We do not work with individual pixels, but with ROIs formed by hun-  
536 dreds to thousands of pixels. Consequently, the SNRs of our measure-

537       ments increase in average to much higher values (several hundreds)  
538       limited by the readout noise of the cameras and dark noise.

- 539       • We assess the accuracy of our measurements by comparing the theoret-  
540       ical reflectance of the calibration target with our measurements. This  
541       comparison shows a variability of 6% with the visible camera and 3%  
542       with the near-infrared.

543       Even though accuracy limitations control our uncertainties, the SNR and  
544       absolute accuracy have different implications on our spectral analyses. We  
545       favour the use of relative spectral criteria, where ratios between wavelengths  
546       of the same spectra are computed (i.e., slopes and band depths). These  
547       relative criteria are not affected by the absolute accuracy that affects the  
548       reflectance at all wavelengths in the same way and are only influenced by the  
549       SNR.

### 550    2.3.2. *Spectral analysis*

551       We study the reflectance spectra of our samples through the reflectance of  
552       the continuum, the depth of the absorption bands, the spectral slopes and the  
553       CaSSIS colours. We have chosen these parameters because they have been  
554       repeatedly used in other spectrophotometric studies (e.g., [30, 42, 36, 69]).  
555       We build on some of their choices and definition of parameters because we  
556       want our data to be comparable with existing data sets.

557       *Reflectance in the continuum.* The reflectance of the continuum allows us to  
558       distinguish bright from dark materials at a specific wavelength. It depends  
559       on various variables such as the single scattering albedo of the material or

560 the size of grains. Both CO<sub>2</sub> and H<sub>2</sub>O ices are bright in the continuum, but  
561 other materials, such as salts, are also bright in the continuum [65]. We have  
562 measured the reflectance of the continuum at 0.940 μm. Langevin et al. [30]  
563 used the reflectance at 1.08 μm as a reference for the reflectance in the contin-  
564 uum, based on a compromise between OMEGA instrumental considerations  
565 and the scattering of aerosols in the Martian atmosphere [30]. The difference  
566 in reflectance between these wavelengths is negligible for the CO<sub>2</sub> and JSC  
567 Mars-1 since they show flat spectra in this region. It is not the case for  
568 water ice, which presents a blue slope in the near-IR, but the difference of  
569 reflectance between these two positions lies within the uncertainties of the  
570 instrument.

*Evaluation of band depths.* The presence and position of absorption bands are specific to the materials (composition and state of the matter), and their depth to the length of the optical path inside the material (linked to the size and/or the amount of material present). We have analysed the absorption signatures of carbon dioxide at 1.435 and 2.281 μm and of water at 1.5 μm. For every band, we have used the evaluators proposed by Langevin et al. [30]. It is not straightforward to assess the strength of the CO<sub>2</sub> signature at 1.435 μm, since it lies close to a CO<sub>2</sub> atmospheric absorption (around 1.444 μm) and it overlaps with the short wavelength side of the water band at 1.5 μm (which starts at 1.38 μm [30]). To minimise the impact of these two features, Langevin et al. [30] defined an evaluator (Eq (1)) from the reflectance (RF) of the spectra at 1.429, 1.385 and 1.443 μm, which, adapted to the sampling

of SCITEAS resulted in 1.432, 1.39 and 1.444  $\mu\text{m}$  respectively.

$$R = \frac{RF(1.432\mu\text{m})}{RF(1.39\mu\text{m})^{0.5} \times RF(1.444\mu\text{m})^{0.5}} \quad (1)$$

Then, Langevin et al. [30] found a relationship between R and the CO<sub>2</sub> strength computed from water-free spectra (Eq (2)).

$$CO_2(1.435\mu\text{m}) = 1.16(1 - R)^{0.92} \quad (2)$$

571 As warned in Langevin et al. [30], the spectral element at 1.444  $\mu\text{m}$  lies in the  
 572 absorption signature of CO<sub>2</sub>, therefore (1-R) underestimates the strength of  
 573 the band.

574 We used Eq (3) and (4) below to evaluate the absorption features at 2.281  
 575  $\mu\text{m}$  (CO<sub>2</sub>) and 1.5  $\mu\text{m}$  (H<sub>2</sub>O) respectively. The values of the wavelengths are  
 576 slightly changed from the original values to adapt SCITEAS sampling.

$$CO_2(2.281\mu\text{m}) = 1 - \frac{RF(2.29\mu\text{m})}{RF(2.226\mu\text{m})^{0.3} \times RF(2.314\mu\text{m})^{0.7}} \quad (3)$$

$$H_2O(1.5\mu\text{m}) = 1 - \frac{RF(1.498\mu\text{m})}{RF(1.390\mu\text{m})^{0.7} \times RF(1.774\mu\text{m})^{0.3}} \quad (4)$$

577 As the band depth is defined as a ratio of two values of reflectance, the  
 578 uncertainty on the band depth is only affected by the SNR.

579 *Spectral slopes.* The spectral slopes indicate how reflectance depends on the  
 580 wavelength. They give us an idea of the colour of the materials, and is useful  
 581 to identify the way in which materials are mixed [56]. We have assessed the  
 582 spectral slopes with Eq (5).  $\lambda_1$  and  $\lambda_2$  have been set to 0.445 and 0.745  $\mu\text{m}$   
 583 in the visible and 1.1 and 1.7  $\mu\text{m}$  in the near-infrared.  $RF_{\lambda_1}$  and  $RF_{\lambda_2}$  refer  
 584 to the values of reflectance at  $\lambda_1$  and  $\lambda_2$  respectively.

$$S_r = \frac{RF_{\lambda_2} - RF_{\lambda_1}}{RF_{\lambda_1}(\lambda_2 - \lambda_1)} \times 10^4 \quad (\%/100nm) \quad (5)$$

585 As for the band depth calculation, the relative uncertainties are therefore  
 586 only affected by the SNR.

587 Throughout this study, we use the terms red, blue and flat slopes. A  
 588 spectrum (or a region of a spectrum) has a red slope when its reflectance  
 589 increases towards longer - or red- wavelengths. Red slopes imply positive  
 590 spectral slope values, measured in %/100 nm. A spectrum (or a region of  
 591 a spectrum) has a blue slope when its reflectance increases towards shorter  
 592 - or blue- wavelengths. Blue slopes imply negative spectral slope values.  
 593 A spectrum (or a region of a spectrum) is flat when it shows a constant  
 594 reflectance, or spectral slope values  $\sim 0$  %/100 nm.

595 *Colour composites.* In the majority of cases, we present the spectral criteria  
 596 averaged per ROI. In some cases, however, we also show the spatial varia-  
 597 tion of these criteria by showing the values per pixel. For that, we can either  
 598 produce monochromatic images where the signal represents a particular spec-  
 599 tral criterion, or we can combine three spectral criteria in RGB composites.  
 600 When choosing the latter, we stretch each channel separately to emphasise  
 601 the colours. We indicate the stretching applied to each channel with each  
 602 RGB composite.

### 603 2.3.3. Colour analysis

604 The Colour and Stereo Surface Imaging System (CaSSIS, [70]) is the  
 605 visible imager of the Exomars Trace Gas orbiter (EM-TGO). It consists of a 4-  
 606 mirrors telescope with a focal length of 880mm, a 2k x 2k pixels CMOS sensor

607 and a rotation mechanism to align the telescope and sensor with respect to  
608 the ground track and obtain nearly-simultaneous stereo images of the surface.  
609 On top of the CMOS sensor, four broadband bandpass filters are mounted  
610 to image the surface in four colours. The respective filter names, effective  
611 central wavelengths and bandwidths (in nm) are: BLU (494.8, 133.6), PAN  
612 (678.2, 231.9), RED (836.0, 98.5), and NIR (939.3, 121.8). Because of the non  
613 Sun-synchronous orbit of TGO and the high sensitivity of the instrument,  
614 CaSSIS is able to observe the surface at variable local Solar times throughout  
615 the seasons and collects a unique dataset to study the diurnal and seasonal  
616 Martian volatiles cycles.

617 The simulated CaSSIS colours inform us on the possibilities and limita-  
618 tions of the instrument when it comes to detecting and distinguishing CO<sub>2</sub>  
619 and H<sub>2</sub>O ices. It also provides us with prior knowledge to target the obser-  
620 vations of the Martian surface. We have convolved the data measured with  
621 SCITEAS with the spectral response of the instrument [71]. This methodol-  
622 ogy is automatised in the calibration software of SCITEAS and was detailed  
623 in Yoldi et al. [56]. Briefly, it is a process in which we take into account  
624 (i) the illumination conditions at an average Sun-Mars distance and a simu-  
625 lated incidence angle, and (ii) the specificities of CaSSIS (angular aperture of  
626 the telescope, area and reflectivity of the mirror, quantum efficiency, trans-  
627 mission of the filters, etc.), to simulate the reflectance that would have been  
628 measured by CaSSIS from samples like ours.

629 To compute the parameters introduced so far (reflectance in the contin-  
630 uum, indices and spectral slopes), we need to know the reflectance of the  
631 samples at specific wavelengths. However, to simulate the CASSIS colours,

632 we need to know the reflectance of the samples in the spectral intervals that  
633 correspond to each filter (BLU, PAN, RED or NIR). The more measurements  
634 we have in an interval, the more accurate our simulations are. That is why  
635 the CaSSIS colours are the only spectral parameter that we derive from hy-  
636 perspectral measurements and therefore, they represent the samples when  
637 they have already undergone sintering and sublimation.

638 Note that the bandpass filters of CaSSIS were designed to be very close  
639 to those of HiRISE with the infrared filter of HiRISE (IR) split into the RED  
640 and NIR filters of CaSSIS to provide additional sensitivity to iron-bearing  
641 mineralogy. Therefore, nearly all observations valid for the CaSSIS filters are  
642 also relevant for HiRISE.

### 643 **3. Results**

#### 644 *3.1. Pure CO<sub>2</sub> ice*

645 Fig 8 shows the reflectance spectra and their byproducts for various size  
646 distributions of CO<sub>2</sub> ice. Fig 8a and Fig 8b evince that the reflectance of the  
647 samples is inversely proportional to the size of their grains. The differences  
648 in reflectance between Fig 8a and Fig 8b are due to the sintering and/or  
649 sublimation of the finest particles of CO<sub>2</sub> ice during the experiments. Fine  
650 grains are more affected by this morphological evolution. The slab shows  
651 relatively low reflectance ( $\sim 0.5$ ) in the continuum, which suggests that part  
652 of the photons crossed the slab and reached the black sample holder. Kieffer  
653 [49] reports that water frost causes reflectance to peak at 1.8 and 2.24  $\mu\text{m}$ ;  
654 we do observe variations around those wavelengths between the multi- and  
655 hyperspectral measurements in, for instance, the slab.

656 The strength of the water index at 1.5  $\mu\text{m}$  (Fig 8c) indicates that, exposed  
657 to the same conditions of relative humidity and temperature, the smallest  
658 particles ( $< 200 \mu\text{m}$ ) cold-trapped more water frost than larger size fractions.  
659 Granular ices present lower CO<sub>2</sub> indices than the slab as the path of the  
660 photons is longer in continuous media. Both CO<sub>2</sub> indices (at 1.435 and  
661 2.281  $\mu\text{m}$ ) remain relatively constant (around 0.1 and 0, respectively) for the  
662 particulate samples.

663 The VIS and NIR spectral slopes are relatively flat (i.e., around 0 %/100  
664 nm) for all the CO<sub>2</sub> samples (Fig 8d). The trapped water frost explains the  
665 small shift of particulate CO<sub>2</sub> ice towards blue slopes ( $\sim -1 \text{ \%}/100 \text{ nm}$ );  
666 it was shown in Yoldi et al. [56] that low amounts of water frost on samples  
667 suffice to lower their visible slopes to negative values. This particular spectral

668 behaviour was also already modeled by [72] and [19] with similar results.

669 Finally, we show in Fig 8e the simulated CaSSIS colours. Because we  
670 obtain the CaSSIS colours from the hyperspectral measurements, the samples  
671 have already evolved. For this reason, the CaSSIS colours do not show a  
672 large difference in reflectance between the fine and the coarse ice grains. We  
673 see no significant difference of reflectance between measurements within the  
674 different filters of CaSSIS.

### 675 *3.2. CO<sub>2</sub> slab with water frost*

676 Fig 9 shows the reflectance spectra and their byproducts for three ROIs  
677 drawn on the CO<sub>2</sub> slab covered with water frost (Fig 9a). ROI #1 is the  
678 one with most water frost ( $\sim 400 \mu\text{m}$  thickness), and ROI #3 the one with  
679 the least ( $\sim 75 \mu\text{m}$  thickness). For comparison purposes, we have added the  
680 spectrum of the slab shown in Fig 8, on which we did not condense any water  
681 intentionally but is still slightly affected by water frost ( $\sim 25 \mu\text{m}$ ).

682 ROIs with more water frost condensed show high reflectance levels (Fig 9a  
683 and Fig 9b). Compared to the slab that had not been exposed to atmospheric  
684 water, ROI #3 shows slightly lower reflectance. We attribute this small  
685 variation to a putative difference in the roughness of the ice surface caused  
686 by the outdoor exposure of the CO<sub>2</sub> slab. Fig 9a and Fig 9b do not show  
687 great differences in the absolute reflectance levels, as slabs do not evolve  
688 during the experiments as much as small particles do.

689 The H<sub>2</sub>O indices at  $1.5 \mu\text{m}$  follow the amount of water frost in each  
690 ROI (Fig 9c). Both CO<sub>2</sub> indices are negatively correlated with water frost  
691 thickness, as fewer photons reach the CO<sub>2</sub> slab due to scattering by the fine-  
692 grained H<sub>2</sub>O frost at the surface. ROI #3 shows slightly higher indices than

693 the water frost-free slab, which can as well be explained by differences in the  
694 thickness of the slabs.

695 We see in Fig 9d that the VIS slope is slightly more sensitive to the amount  
696 of water frost condensed on the slabs than the NIR slope. The presence of  
697 water frost turns the visible spectral slope blue.

698 Measured with CaSSIS, the ROIs with water frost would appear up to  
699 20% brighter than the non-contaminated slab (Fig 9e). Because of the blue  
700 slope induced by water frost, ROIs with more frost appear brighter in the  
701 BLU filter ( $\sim 400 - 550$  nm) than in the red ones (PAN:  $\sim 550 - 800$  nm;  
702 RED:  $\sim 800 - 900$  nm; RED:  $\sim 900 - 1100$  nm).

### 703 3.3. $CO_2$ and $H_2O$ ice intimate mixtures

704 Fig 10 shows the reflectance spectra of the  $CO_2$  (frost, crushed) and  $H_2O$   
705 (fine, coarser) intimate mixtures. For all the different combinations, we see  
706 that the pure  $CO_2$  sample is not the brightest. This is the result of the  
707 difficulties of mixing  $CO_2$  ice with other components discussed previously.

708 We see that water ice affects the reflectance spectra of the mixtures out  
709 of proportion to its concentration; water concentrations as low as 3 wt%  
710 are enough to dominate the spectrum. We see different behaviours in the  
711 continuum and the absorptive regions of the spectra. The reflectance of the  
712 continuum and other weak absorption features of water seems to be con-  
713 trolled by the texture (grain size, shape, surface roughness, density...) of  
714 the samples, which are not homogeneous due to the formation of agglomer-  
715 ates (see Fig 4a). The reflectance in the spectral regions of the absorption  
716 bands of water (centred at 1.5 and 2.0  $\mu\text{m}$ ), however, is more sensitive to the  
717 composition of the samples.

718 Fig 11 shows the reflectance spectra of the CO<sub>2</sub> (frost, crushed) and H<sub>2</sub>O  
719 (fine, coarser) intimate mixtures. We have added the pure spectra of the fine  
720 and coarser grained H<sub>2</sub>O ices for comparison.

721 Overall, we observe that the samples with CO<sub>2</sub> frost (10-100 μm) subli-  
722 mate faster than those with crushed CO<sub>2</sub>. By the shape of the CO<sub>2</sub> absorp-  
723 tion bands within that of water ice at 2.0 μm, we see that CO<sub>2</sub> ice resists  
724 sublimation better when mixed with coarser H<sub>2</sub>O ice particles than with finer  
725 ones.

726 Comparing Fig 10 and Fig 11, we see that samples with more water show  
727 a greater drop in the reflectance from the multi- to the hyperspectral figures.  
728 As CO<sub>2</sub> ice sublimates, the CO<sub>2</sub> - to - H<sub>2</sub>O decreases and water ice forms a  
729 lag that dominates the spectrum.

730 Fig 3.3 shows the CO<sub>2</sub> and H<sub>2</sub>O indices for intimate mixtures with CO<sub>2</sub>  
731 frost (Fig 3.3a) and crushed CO<sub>2</sub> (Fig 3.3b). The H<sub>2</sub>O indices of mixtures  
732 with 5 wt.% of water ice are already half of that of the same mixtures with  
733 100 wt% of water ice.

734 The CO<sub>2</sub> indices decrease with the concentration of CO<sub>2</sub>. A reduction of  
735 10 wt% of CO<sub>2</sub> ice within the mixtures reduces the index at 1.4 μm by ~38%  
736 for the samples with CO<sub>2</sub> frost and by ~33% for the samples with crushed  
737 CO<sub>2</sub>. The index at 2.281 μm is so weak that it cannot be measured in the  
738 majority of the cases.

739 We see that, in general, the VIS and NIR spectral slopes are bluer with  
740 increasing concentration of H<sub>2</sub>O ice in the mixture (Fig 13a and 13b).

741 As seen in Fig 10 and Fig 11, the visible part of the spectra is dominated  
742 by the texture of the samples rather than by their composition. Consequently,

743 the reflectance measured with CaSSIS (Fig 13c and 13e) does not overall  
744 follow the composition of the samples. As CO<sub>2</sub> ice covers water ice and the  
745 spectral slope becomes neutral, the different filters measure similar values of  
746 reflectance.

#### 747 3.4. Crushed CO<sub>2</sub> ice and JSC Mars-1 intimate mixtures

748 Fig 14a and Fig 14b show that the reflectance of the intimate mixtures  
749 of JSC Mars-1 and crushed CO<sub>2</sub> drops as the amount of ice decreases. Com-  
750 pared to the spectra of crushed ice of same size distribution (Fig 8a, Fig 8 b),  
751 the pure CO<sub>2</sub> ice shown here is about 20% darker. This can be due to the  
752 broad size distribution that we are using (400-800 μm); if the histogram of  
753 grain size distribution peaks towards 800 μm, then the reflectance is expected  
754 to be weaker than if it peaks towards 400 μm. We also see that samples which  
755 initially contained up to 35 wt% of CO<sub>2</sub> ice only show a weak CO<sub>2</sub> absorption  
756 around 2.29 μm. In the VIS, we can identify the red slope characteristic of  
757 JSC Mars-1 when the weight of dust is only a quarter of that of the sample.

758 We analyse in Fig 14c the CO<sub>2</sub> and H<sub>2</sub>O signatures of the samples. The  
759 spectrum of JSC Mars-1 shown here was not measured together with the rest  
760 of the samples, and therefore its H<sub>2</sub>O index reflects its degree of hydration.  
761 The water index shows no correlation between the cold-trapped water frost  
762 and the CO<sub>2</sub> wt%. Instead, we attribute the variation in cold-trapped water  
763 frost to the process of filling of the sample holders, which was longer than  
764 usual as there were more samples to fill. Both CO<sub>2</sub> signatures tend to increase  
765 with the weight percentage of CO<sub>2</sub>; as observed previously, the signature at  
766 1.435 μm is stronger than the one at 2.281 μm.

767 Fig 14d shows that the VIS slope of the sample with 5 wt% of CO<sub>2</sub> ice is

768 reduced by a 50% compared to JSC Mars-1, and it continues decreasing as the  
769 percentage of carbon dioxide increases. In the NIR, the spectral slope remains  
770 flat-to-bluish, oscillating from 0 to -4 %/100 nm following the amount of  
771 water frost condensed at the surface of the samples.

772 Measured with CaSSIS (Fig 14e), the presence of JSC Mars-1 results in  
773 reflectance measurements in the BLU filter around 30% weaker than in other  
774 filters. This gap between the reflectance measured in the different filters  
775 narrows as the percentage of ice increases until it disappears entirely for the  
776 pure CO<sub>2</sub> sample. With 75wt% of CO<sub>2</sub> ice, the BLU filter still measures  
777 20% lower reflectance than the other ones. This value is similar to the ones  
778 measured in [56] for water ice and JSC Mars-1 intimate mixtures.

### 779 3.5. Sublimation series of the ternary mixtures

780 Fig 15 is a 2x2 matrix of plots showing the evolution of the reflectance  
781 spectra of the ternary mixtures as the CO<sub>2</sub> and H<sub>2</sub>O ices sublimated. The  
782 rows correspond to the size of water ice (fine or coarser) and the columns to  
783 the texture of the samples (compact or powder). The four samples initially  
784 had the same composition: 96.8 wt% of CO<sub>2</sub> frost, 3 wt% of water ice and  
785 0.2 wt% of JSC Mars-1 ( particles smaller than 100 μm).

786 We observe similarities with the binary mixtures, namely: 1) A shape of  
787 the spectra dominated by water ice, even if present at low concentrations.  
788 2) A first, relatively abrupt, darkening of the sample (between  $t_0$  and  $t_1$ ),  
789 explained by the quick sublimation of cold-trapped water frost. 3) A progres-  
790 sive change in the shape of the water bands towards broader and less complex  
791 bands, indicating the warming up of the samples. 4) The VIS (400-950nm)  
792 shows greater variation in these plots, since that region is more sensitive to

793 changes in the texture.

794 The compacted samples initially show a higher reflectance than the pow-  
795 dered ones, partly explained by the trapped water frost.

796 We observe a non-intuitive behaviour of the absorption band of CO<sub>2</sub>  
797 around 2 μm in the samples with fine H<sub>2</sub>O ice, which does not seem to occur  
798 with coarser H<sub>2</sub>O ice. The band decreases to a minimum at t<sub>3</sub> to later on grow  
799 again and be noticeable by the end of the experiment, when the temperature  
800 of the air above the sample was of 250 K (55 K above the sublimation point  
801 of CO<sub>2</sub> at atmospheric pressure (Fig 7)).

802 The evolution of carbon dioxide and water indices (Fig 16a) shows a  
803 growing H<sub>2</sub>O index at 1.5 μm as CO<sub>2</sub> sublimates. For all the samples, there  
804 is an initial, steep increase of the water index, that slows down after t<sub>3</sub>. As  
805 observed in Fig 15, the evolution of the CO<sub>2</sub> index depends on the size of the  
806 water ice. The CO<sub>2</sub> indices in samples with fine grained water ice decreases  
807 by around half from t<sub>0</sub> to t<sub>4</sub> and stay constant around 0.025 until t<sub>9</sub>. The  
808 CO<sub>2</sub> indices in samples with coarser grained water ice oscillate around 0.075  
809 from t<sub>0</sub> to t<sub>4</sub> and then decrease down to 0.05 until t<sub>9</sub>. After that, the CO<sub>2</sub>  
810 indices of every sample start increasing until the end of the measurement.  
811 We do not detect any absorption at 2.281 μm during the duration of the  
812 experiment.

813 Fig 16b shows the evolution of the visible and near-infrared spectral slopes  
814 of the ternary mixtures. The ternary mixtures are a combination of compo-  
815 nents with different spectral slopes; (i) CO<sub>2</sub> ice, with no slope in both the  
816 VIS and NIR ranges, (ii) H<sub>2</sub>O ice, with blue slopes in the visible (~-1%/100  
817 nm) and near-infrared (SPIPA-A: -8.4%/100 nm, SPIPA-B: -13%/100 nm)

818 spectral ranges, and (iii) JSC Mars-1, red in the visible ( $\sim 140\%/100$  nm)  
819 and flat in the near-infrared range. Because of the neutral slopes of CO<sub>2</sub> ice,  
820 this component only impacts the reflectance slopes by how much it covers or  
821 uncovers the other components.

822 In the visible range of the spectrum, the slopes are expected to become  
823 redder as water ice sublimates and the relative abundance of JSC Mars-1  
824 increases. The ternary mixtures with coarser grained water ice show such  
825 a behaviour, as a dust lag formed with the sublimating ice. The spectral  
826 slopes of ternary mixtures with fine grained H<sub>2</sub>O ice, however, remained  
827 constant around 2.5 %/100 nm during the six hours of the experiment; the  
828 scattering by small ice particles dominated the reflectance. We can assume  
829 that we would have seen the same dust lag after some additional hours of  
830 sublimation. In the same way, the NIR spectral slopes of these samples are  
831 dominated by water ice. Because there is no water absorption associated  
832 with the transient decrease in the spectral slope of the powdered sample  
833 with coarser grained water ice (see Fig 15a) at  $t_8$ , we assume this point to  
834 possibly be an instrumental artefact.

### 835 *3.6. Comparison of criteria. Addition of water ice and dust experiments*

836 We compare now the criteria defined in Section 2 for all the experiments.  
837 We aim to find trends among the samples to eventually identify them in  
838 terms of composition and mixing mode. We used the same strategy in the  
839 first part of this study, where we focused on water ice and dust associations  
840 [56]. Hence, we have added to some of the plots the experiments with water  
841 ice and JSC Mars-1 conducted in Yoldi et al. [56]. We provide here a summary  
842 of the water ice experiments to ease reading of the figure. The corresponding

843 legend is given in Fig 17ii).

- 844 1. *JSCM-1 + Water frost samples*: experiments in which water frost was  
845 condensed onto various size fractions of JSC Mars-1. By sporadically  
846 exposing the samples to the atmosphere, we studied the reflectance of  
847 different thickness of water frost on the regolith.
- 848 2. *Intimate mixtures*: JSC Mars-1 and SPIPA-A or SPIPA-B mixtures.  
849 We mixed the original size distribution of JSC Mars-1 with 10, 35, 50  
850 and 75 wt% of SPIPA-A and SPIPA-B separately.
- 851 3. *Frozen soils*: experiments in which we thoroughly wet various size frac-  
852 tions of JSC Mars-1 and froze them. The result was a matrix of water  
853 ice surrounding the JSC Mars-1 grains. We measured the reflectance  
854 of the samples as ice sublimated.

855 Fig 18a compares the reflectance of the continuum ( $0.940\ \mu\text{m}$ ) to the  $\text{CO}_2$   
856 indices of the samples. For clarity, the X-axis only shows values up to 0.5.  
857 The pure ice samples (blue symbols) occupy reflectance values from  $\sim 1.0$   
858 to 0.5 and  $\text{CO}_2$  indices between 0.1 and 0.3. JSC Mars-1 and crushed  $\text{CO}_2$   
859 intimate mixtures group on the bottom left of the graph, with reflectance  
860 values and  $\text{CO}_2$  indices lower than 0.4 and 0.1 respectively. The ternary  
861 mixtures cover a large range of reflectance values and are grouped on the left  
862 side of the graph with  $\text{CO}_2$  indices lower than  $\sim 0.1$ .

863 We compare in Fig 18b the  $\text{CO}_2$  index and the VIS (top graph) and NIR  
864 (bottom) spectral slopes. The graph at the top is L-shaped. There is a  
865 vertical column around 0-values of the visible spectral slopes formed by pure  
866 ice samples. Samples with JSC Mars-1 fill the horizontal section of the graph

867 with CO<sub>2</sub> index values of 0.1 and a wide range of spectral slopes depending  
868 on their content of JSC Mars-1. For reference, the visible spectral slope of  
869 pure JSC Mars-1 exceeds 100%/100 nm. The graph on the bottom shows a  
870 shrunk, flipped L-shape. This plot differentiates intimate mixtures of CO<sub>2</sub>  
871 and H<sub>2</sub>O mixtures (around -3 and -7 %/100 nm) from pure CO<sub>2</sub> samples  
872 that trapped water frost (around 0 and -2 %/100 nm). Ternary mixtures  
873 show the bluest slope of all samples, ranging from -4 to almost -10 %/100  
874 nm. Intimate mixtures of crushed CO<sub>2</sub> and JSC Mars-1 fall together with  
875 the pure CO<sub>2</sub> samples, except for the points that correspond to samples with  
876 more JSC Mars-1.

877 In Fig 18c, we compare the reflectance in the continuum and the H<sub>2</sub>O  
878 index at 1.5 μm. The experiments with CO<sub>2</sub> and hydrated minerals (JSC  
879 Mars-1), the granular CO<sub>2</sub> that trapped atmospheric water and the exper-  
880 iments where water frost had condensed on a CO<sub>2</sub> slab cluster to the left,  
881 below H<sub>2</sub>O indices of 0.2. The exception is the ROI on the slab that was  
882 completely covered by water frost, whose water index is ~0.25. As seen  
883 previously, this group of experiments presents a wide range of reflectance  
884 values, from ~1.0 for the finest CO<sub>2</sub> grains to 0.2 for the samples containing  
885 high amounts of JSC Mars-1. Intimate mixtures of CO<sub>2</sub> and H<sub>2</sub>O ice form a  
886 group above reflectance values of 0.7 and between H<sub>2</sub>O index of 0.2 and ~0.5.  
887 These points get progressively closer to the values of pure water ice. They do  
888 not, however, follow a linear path since -as seen previously- the reflectance  
889 spectra in the visible is more dependent on the texture of the sample than  
890 on the CO<sub>2</sub>-to-H<sub>2</sub>O ratio. Finally, ternary mixtures are seen at high values  
891 of H<sub>2</sub>O indices (0.4-0.8) and spread reflectance values (0.25-1.0).

892 In Fig 18d, we incorporate the water ice and JSC Mars-1 samples from  
893 Yoldi et al. [56]. CO<sub>2</sub> and JSC Mars-1 intimate mixtures cluster together  
894 with the JSC Mars-1 samples on which water frost condensed, which indicates  
895 that intimate mixtures trapped atmospheric water. Fig 18d also evinces that  
896 CO<sub>2</sub> ice (non-absorptive material) intimately mixed with only a 3 wt% of  
897 water ice shows water indices as strong as JSC Mars-1 (absorptive material)  
898 intimately mixed with 35 wt% of water ice. We also note that as the loose  
899 ternary mixtures sublime, they join the points representing the intimate  
900 mixtures of water ice and JSC Mars-1.

901 In the top graph of Fig 19e, we compare the water index at 1.5 μm with the  
902 VIS spectral slope. The distribution of the points is similar to that observed  
903 in Fig 18b. Here, however, the ternary mixtures are easily distinguishable  
904 from the JSC Mars-1 and CO<sub>2</sub> ice intimate mixtures, since they show high  
905 H<sub>2</sub>O indices (0.4 to 0.7 compared to a maximum of 0.2 for the mixtures  
906 without water ice). This graph also distinguishes between CO<sub>2</sub> samples that  
907 trapped small quantities of atmospheric water and intimate mixtures of CO<sub>2</sub>  
908 and H<sub>2</sub>O ices. The graph on the bottom compares the water index to the  
909 NIR spectral slope: all the samples follow a similar path from flat slopes  
910 towards the slope values of pure water ice.

911 When we add the water experiments (Fig 19f), we see that, for the VIS,  
912 most of the water experiments fill in the gap left by the L-shaped graph drawn  
913 by the CO<sub>2</sub> samples. The JSCM-1/water frost experiments overlap again the  
914 CO<sub>2</sub> and JSC Mars-1 intimate mixtures. Looking at the NIR spectral slopes,  
915 the JSC Mars-1 and water frozen soils fall outside the trend drawn by the  
916 CO<sub>2</sub> experiments.

917 Finally, we compare in Fig 19g the reflectance measured in the RED filter  
918 of CaSSIS to the PAN/RED and BLU/RED filter ratios. We have zoomed  
919 into the X-axis of the PAN/RED band ratio. We do not include in these  
920 graphs the ternary mixtures since we only performed quick scans with those  
921 samples, which does not allow us to perform CaSSIS colour simulations (see  
922 Section 2). Both graphs allow us to separate the samples bearing JSC Mars-1  
923 from those of pure ice. All the pure ice samples gather around band ratios  
924 of 1, samples with pure water being redder than the ones with CO<sub>2</sub>. When  
925 we add the water ice samples to the plot (Fig 19h), CO<sub>2</sub> and JSC Mars-1  
926 intimate mixtures do not align with the water ice and JSC Mars-1 intimate  
927 mixtures. Instead, intimate mixtures of CO<sub>2</sub> and JSC Mars-1 fall in between  
928 the intimate mixtures of water ice and JSC Mars-1 and the frozen soils. This  
929 is because CO<sub>2</sub> ice has a redder spectral slope than water ice. Hence, the  
930 intimate mixtures with CO<sub>2</sub> and JSC Mars-1 plot below and parallel to the  
931 intimate mixtures with H<sub>2</sub>O ice and JSC Mars-1.

## CO<sub>2</sub> ice.

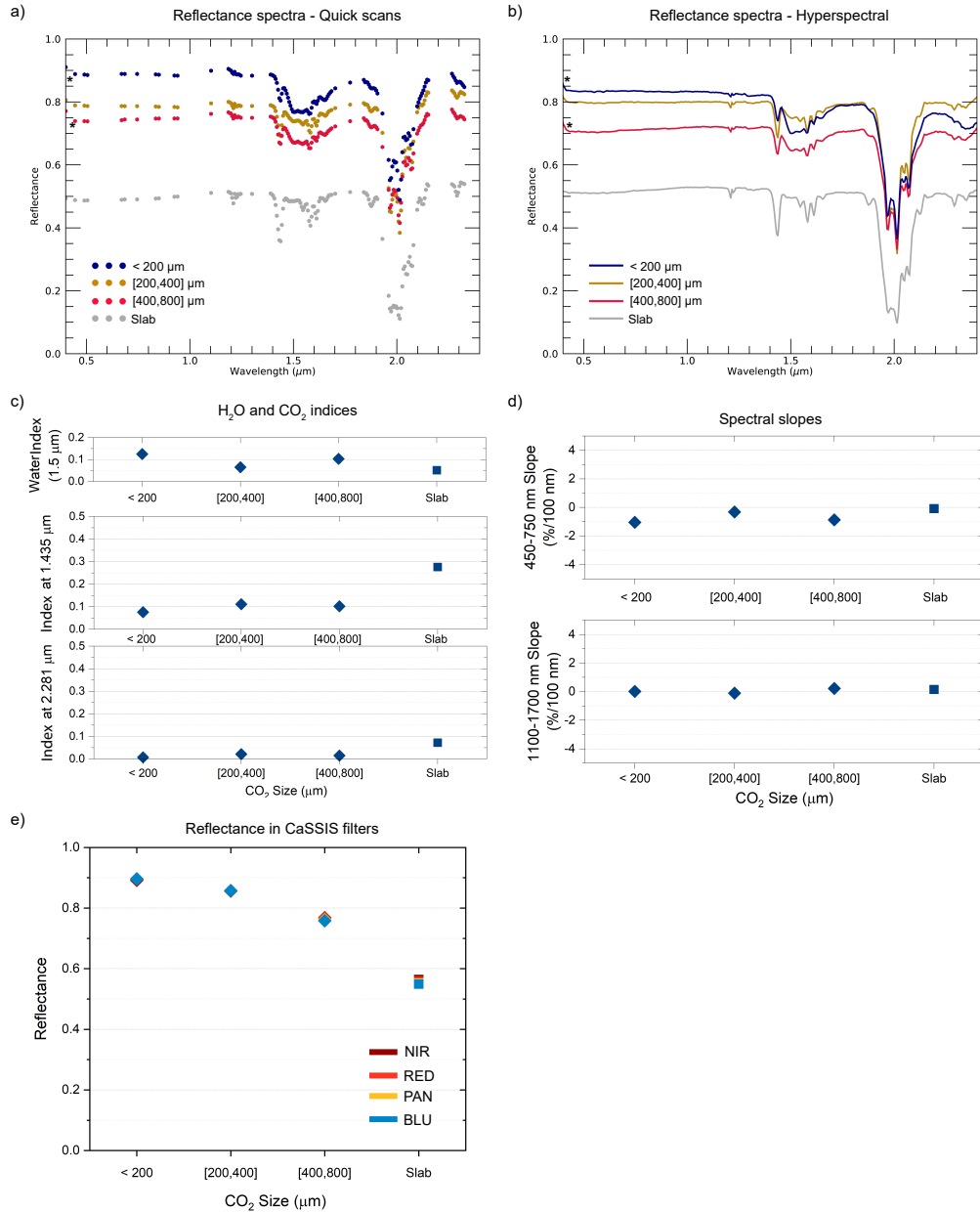


Figure 8: a) Multispectral reflectance spectra for various CO<sub>2</sub> grain sizes. b) Hyperspectral reflectance spectra for various CO<sub>2</sub> grain sizes. c) Strength of various absorption features: the one from H<sub>2</sub>O at 1.5 μm (indicative of the cold-trapped water) and the ones at 1.435 and 2.281 μm of CO<sub>2</sub> ice. d) VIS and NIR spectral slopes of the samples. e) Simulated reflectance measured in the CaSSIS filters. \* Stars indicate calibration artifacts at the shortest wavelengths. All CO<sub>2</sub> samples appear contaminated by H<sub>2</sub>O frost with estimated thicknesses of 100 μm, 50 μm, 75 μm and 25 μm (from the finest to the coarsest size fraction) based on the strength of the 1.5 μm feature.

### Water frost over CO<sub>2</sub> slab.

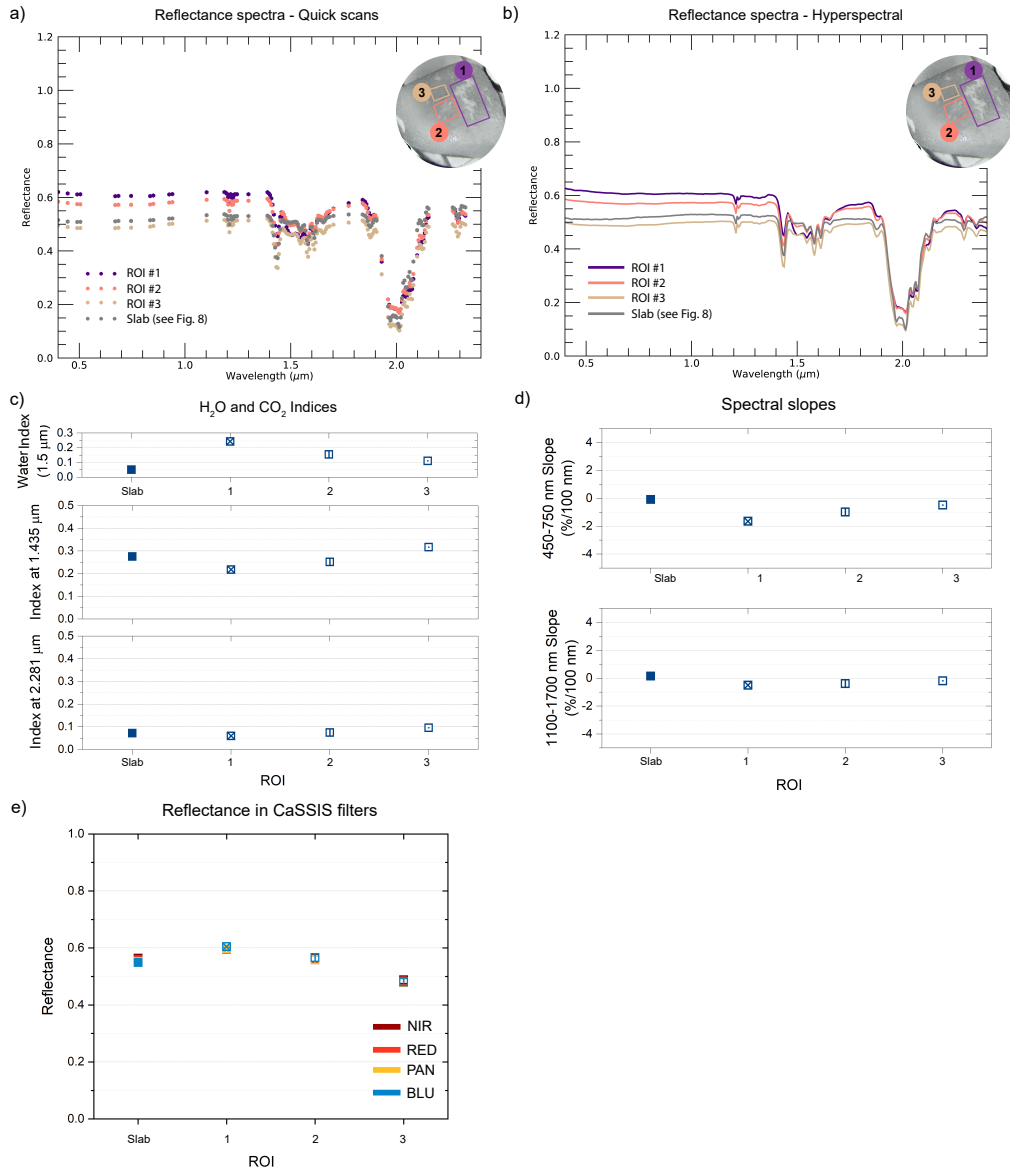


Figure 9: Water frost over CO<sub>2</sub> slab with different amount/thickness of frost within three ROIs identified on the RGB colour composite. a) Multispectral reflectance spectra of the ROIs. b) Hyperspectral reflectance spectra of the ROIs. c) Strength of various absorption features: the one from H<sub>2</sub>O at 1.5 μm and the ones at 1.435 and 2.281 μm from CO<sub>2</sub> ice. d) VIS and NIR spectral slopes of the ROIs. e) Simulated reflectance measured in the CaSSIS filters. Based on the observed strengths of the 1.5 μm band compared to earlier experimental work, we estimate the frost thicknesses in the three ROIs ( 1, 2 and 3) to be 400, 150 and 75 μm, respectively.

## CO<sub>2</sub> and H<sub>2</sub>O ice. Intimate mixtures I

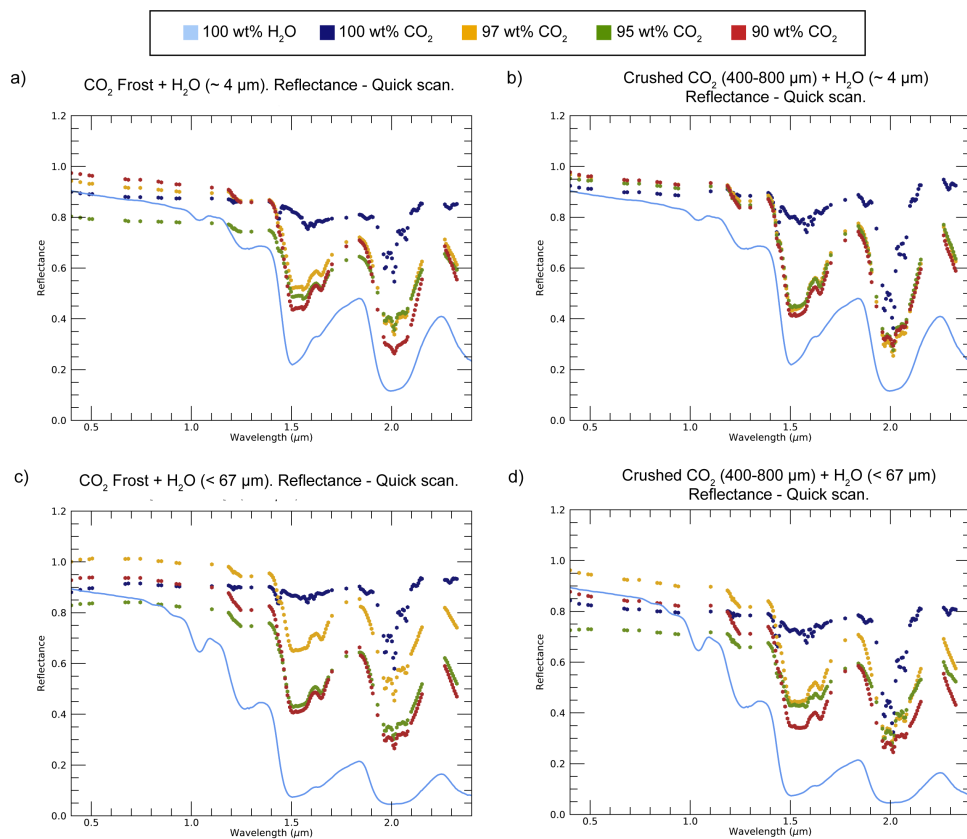


Figure 10: Multispectral (quick scans) spectra of intimate mixtures of CO<sub>2</sub> and H<sub>2</sub>O ices. The legend shows the CO<sub>2</sub> content of each sample. a) CO<sub>2</sub> frost with fine grained H<sub>2</sub>O ice (~ 4 μm). b) Crushed CO<sub>2</sub> with fine grained H<sub>2</sub>O ice (~ 4 μm). c) CO<sub>2</sub> frost with coarser grained H<sub>2</sub>O ice (< 67 μm). d) Crushed CO<sub>2</sub> with coarser grained H<sub>2</sub>O ice (< 67 μm).

## CO<sub>2</sub> and H<sub>2</sub>O ice. Intimate mixtures II

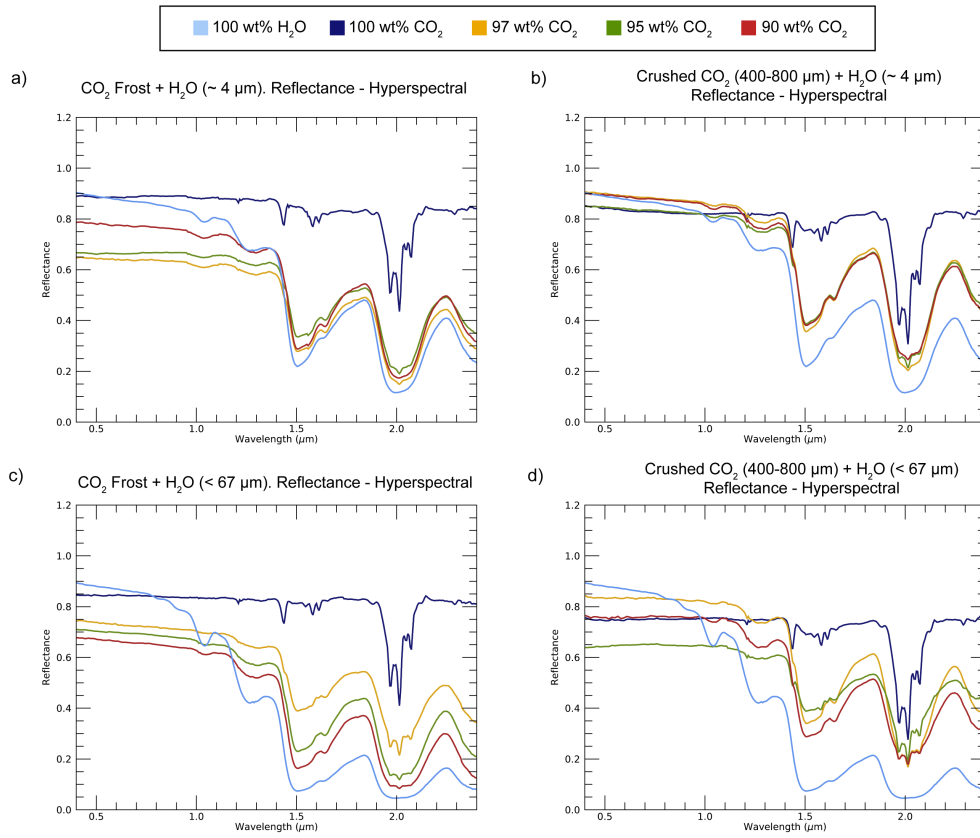


Figure 11: Hyperspectral spectra of intimate mixtures of CO<sub>2</sub> and H<sub>2</sub>O ices. The legend shows the CO<sub>2</sub> content of each sample. a) CO<sub>2</sub> frost (10-100 μm) with fine grained H<sub>2</sub>O ice (~ 4 μm). b) Crushed CO<sub>2</sub> with fine grained H<sub>2</sub>O ice (~ 4 μm). c) CO<sub>2</sub> frost with coarser grained H<sub>2</sub>O ice (~ 67 μm). d) Crushed CO<sub>2</sub> with coarser grained H<sub>2</sub>O ice (~ 67 μm).

### CO<sub>2</sub> and H<sub>2</sub>O ice. Intimate mixtures III

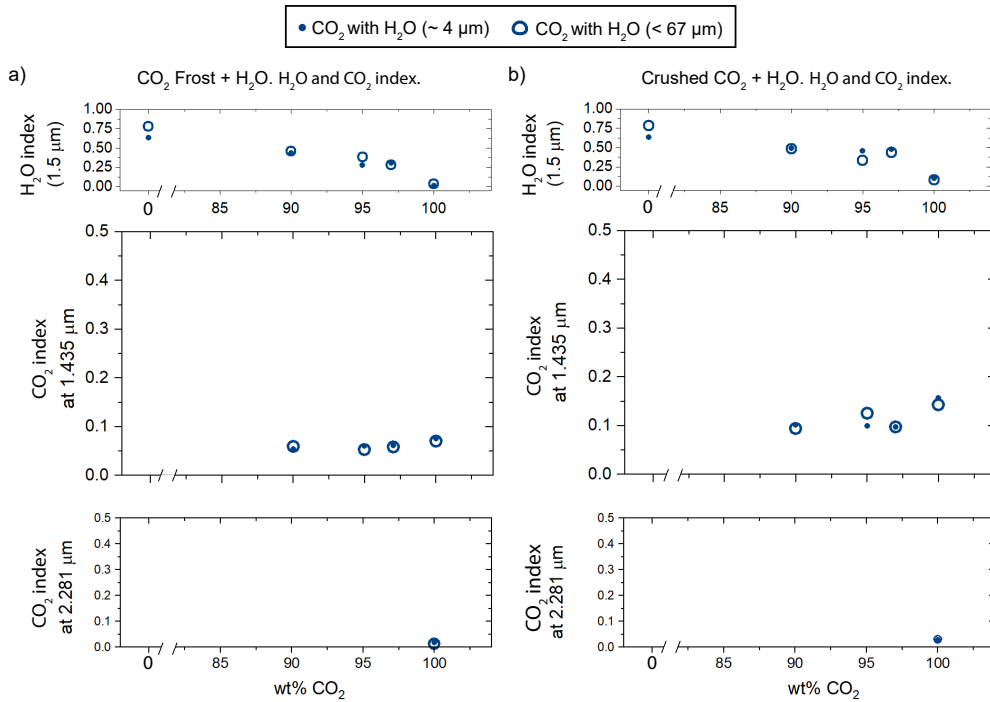


Figure 12: A

analysis of different spectral criteria for intimate mixtures of CO<sub>2</sub> and H<sub>2</sub>O ices in the form of H<sub>2</sub>O ice particles of either ~ 4 μm or ~ 67 μm (full vs. open symbols), a) Using CO<sub>2</sub> frost (10-100 μm). b) Using crushed CO<sub>2</sub> (400-800 μm)

## CO<sub>2</sub> and H<sub>2</sub>O ice. Intimate mixtures IV

● CO<sub>2</sub> with H<sub>2</sub>O (~ 4 μm)    ○ CO<sub>2</sub> with H<sub>2</sub>O (< 67 μm)

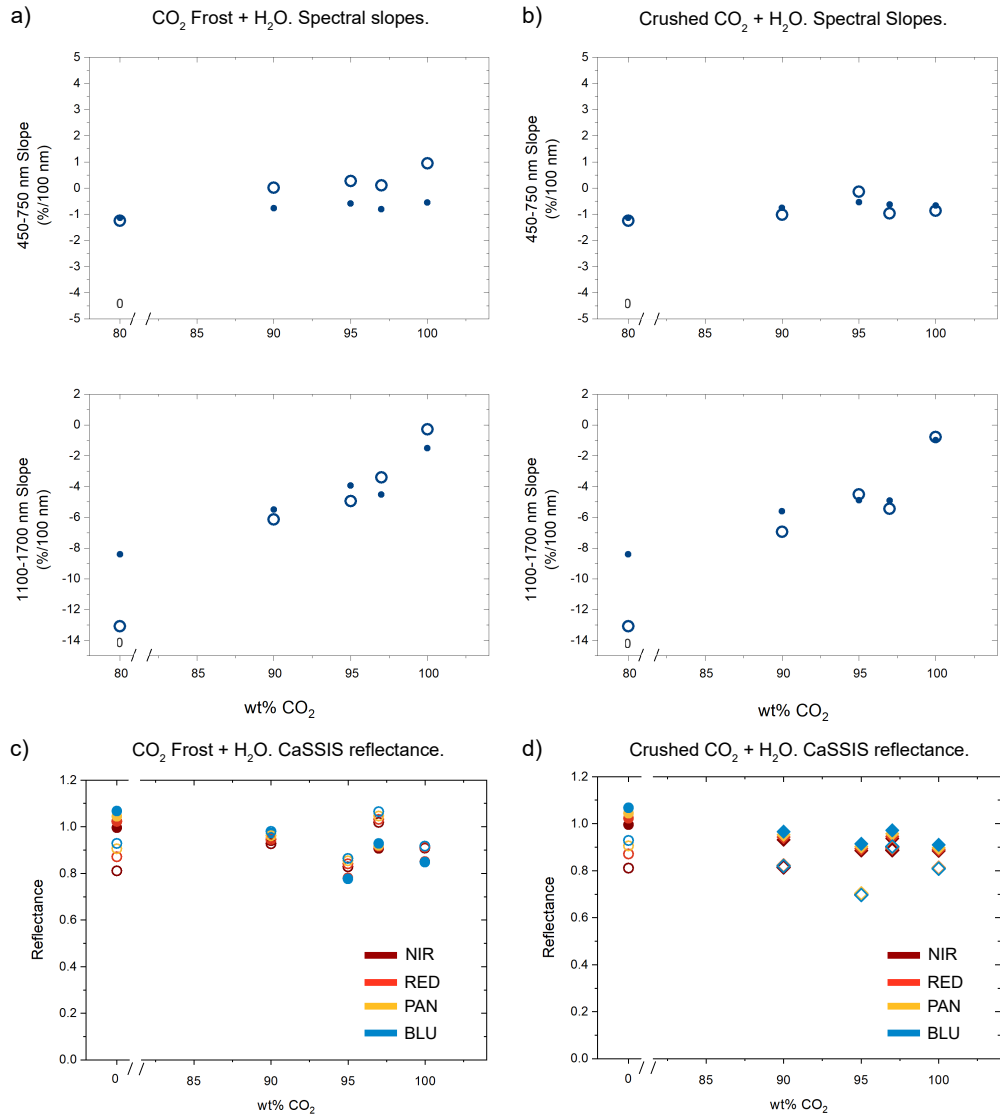


Figure 13: Analysis of spectral criteria for intimate mixtures of H<sub>2</sub>O ice and CO<sub>2</sub> ice in the form of left) frost (10-100 μm) or right) crushed particles between 400 and 800 μm. a) and b) Visible (top) and near-IR (bottom) spectral slopes. c) and d) Simulated reflectance with the CaSSIS filters.

Crushed CO<sub>2</sub> (400-800 μm) and JSCM-1 intimate mixtures.

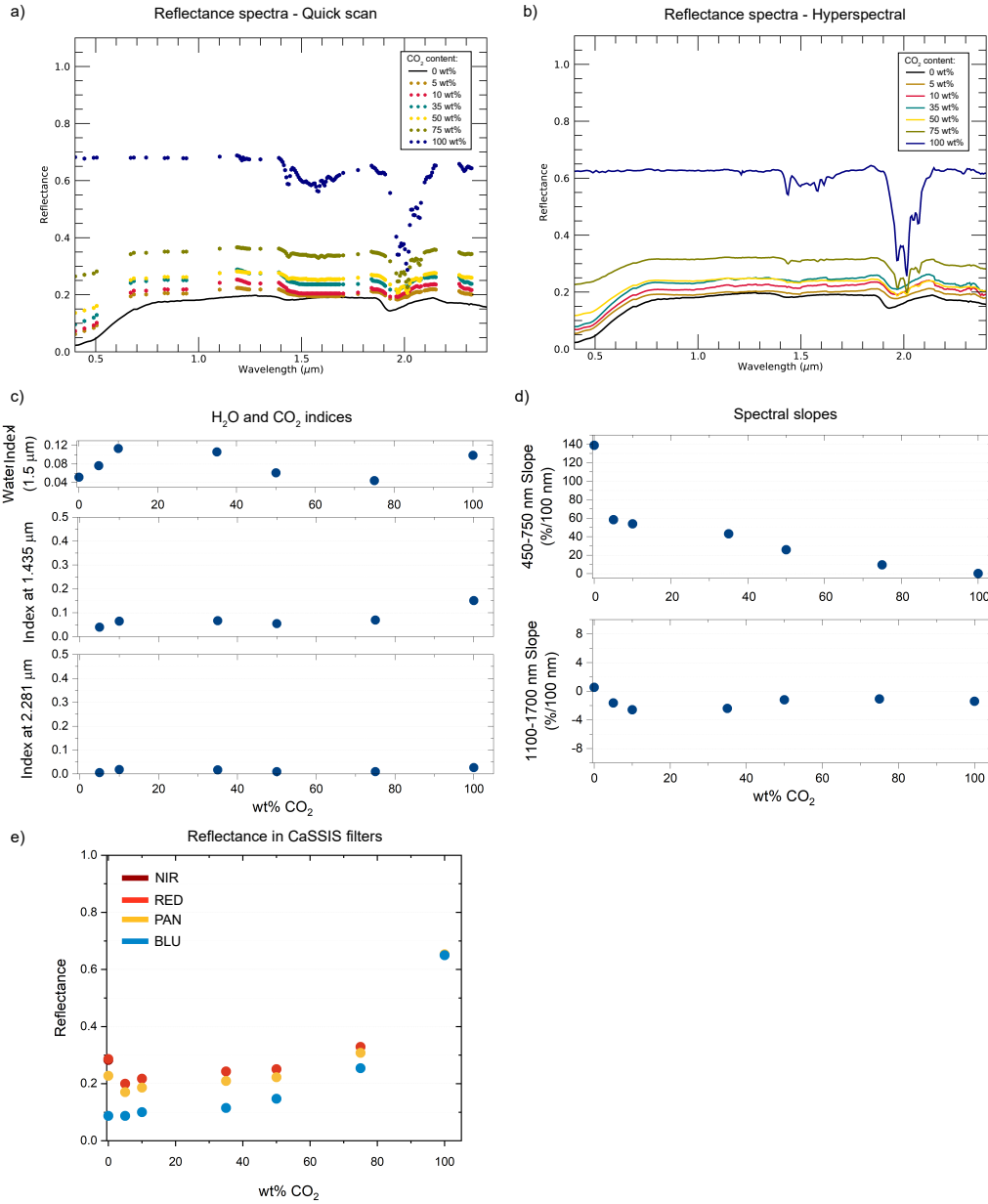


Figure 14: Reflectance analysis of crushed CO<sub>2</sub> ice and JSC Mars-1 intimate mixtures. a) Multispectral (quick scans) reflectance spectra. b) Hyperspectral reflectance spectra c) Strength of various absorption features: the one from H<sub>2</sub>O at 1.5 μm (indicative of the cold-trapped water) and the ones at 1.435 and 2.281 μm from CO<sub>2</sub> ice. d) VIS and NIR spectral slopes of the samples. e) Simulated reflectance measured in the CaSSIS filters.

Sublimation series of CO<sub>2</sub> and H<sub>2</sub>O ice with JSCM-1.

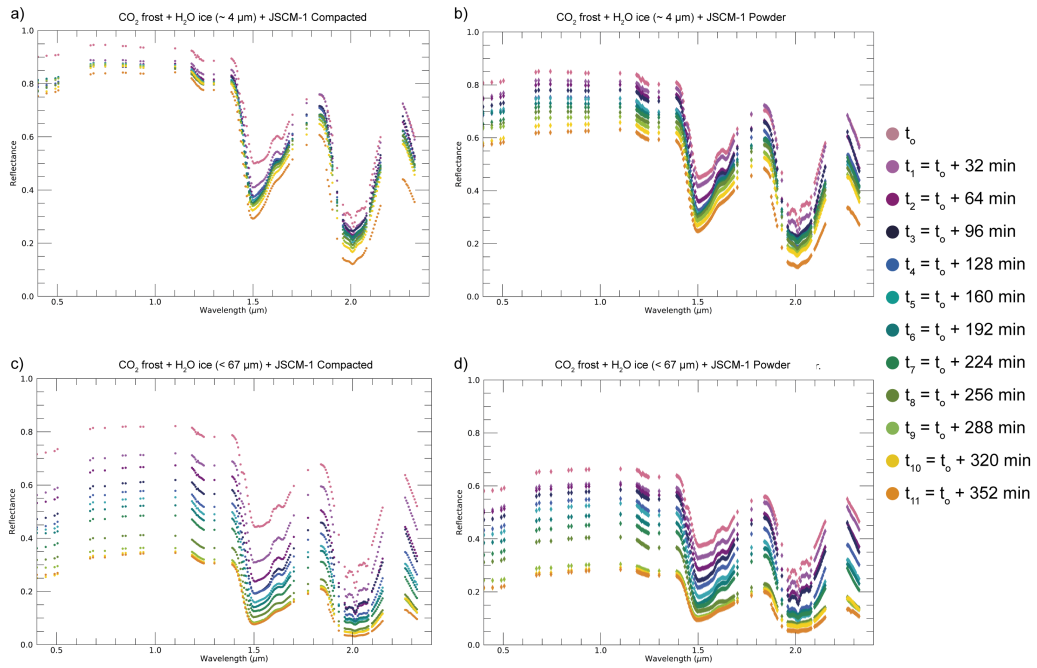


Figure 15: Reflectance spectra of ternary intimate mixtures (CO<sub>2</sub> and H<sub>2</sub>O ice with JSC Mars-1). a) Compacted mixture of CO<sub>2</sub> frost (10-100 μm), fine grained H<sub>2</sub>O ice (~4 μm) and JSC Mars-1. b) Powdered mixture of CO<sub>2</sub> frost, fine grained H<sub>2</sub>O ice and JSC Mars-1. c) Compacted mixture of CO<sub>2</sub> frost, coarser grained H<sub>2</sub>O ice (~67 μm) and JSC Mars-1. d) Powdered mixture of CO<sub>2</sub> frost, coarser grained H<sub>2</sub>O ice and JSC Mars-1.

### Sublimation series of CO<sub>2</sub> and H<sub>2</sub>O ices with JSC Mars-1

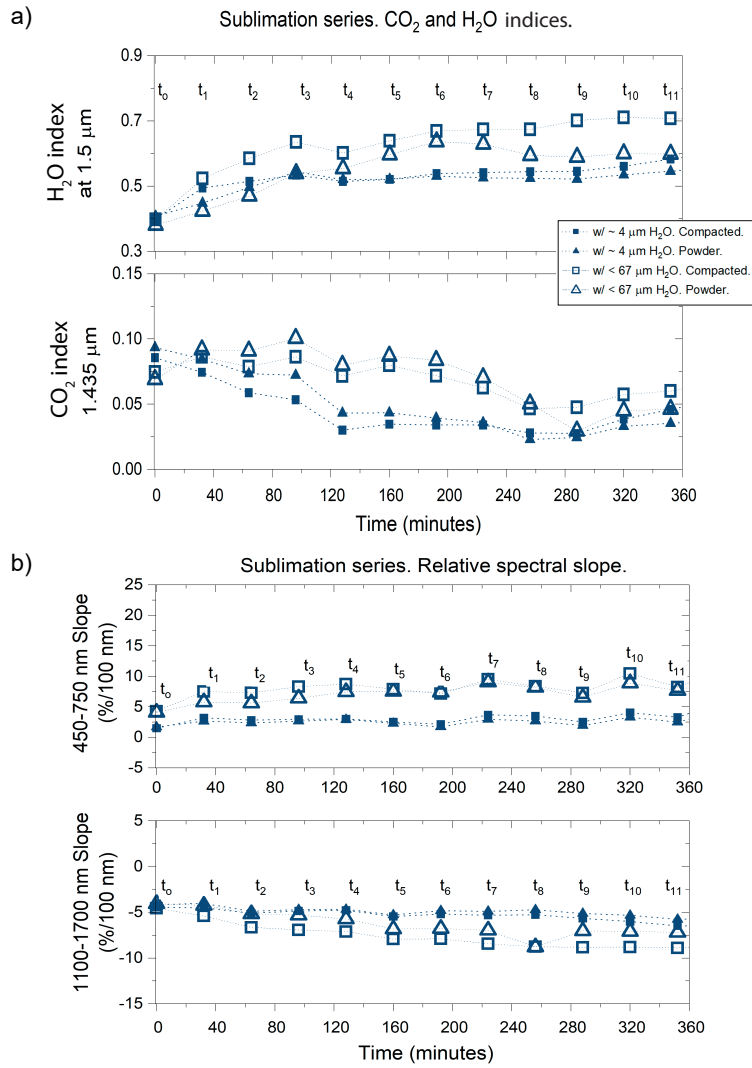


Figure 16: Analysis of spectral criteria of ternary mixtures of CO<sub>2</sub>/H<sub>2</sub>O ice with JSC Mars-1. a) Analysis of the water (1.5 μm) and carbon dioxide (1.435 and 2.281 μm) indices. b) VIS (top) and NIR (bottom) spectral slopes.

- i) ■ CO<sub>2</sub> Slab
- ◆ CO<sub>2</sub> Granulated
- ⊠ CO<sub>2</sub> Slab with H<sub>2</sub>O frost
- ◊ Intimate mixture: CO<sub>2</sub> + H<sub>2</sub>O
- ◆ Intimate mixture: CO<sub>2</sub> + JSCM-1
- Ternary mixture: CO<sub>2</sub> + H<sub>2</sub>O + JSCM-1
- ii) ● H<sub>2</sub>O Granulated
- × H<sub>2</sub>O Frost over JSCM-1
- Intimate mixture: JSCM-1 + H<sub>2</sub>O
- Frozen soil JSCM-1
- ▲ JSCM-1

Figure 17: Legends applicable to Figs. 18 and 19. i) Legend applicable to the CO<sub>2</sub> experiments. ii) Legend applicable to the H<sub>2</sub>O experiments, imported from [56]

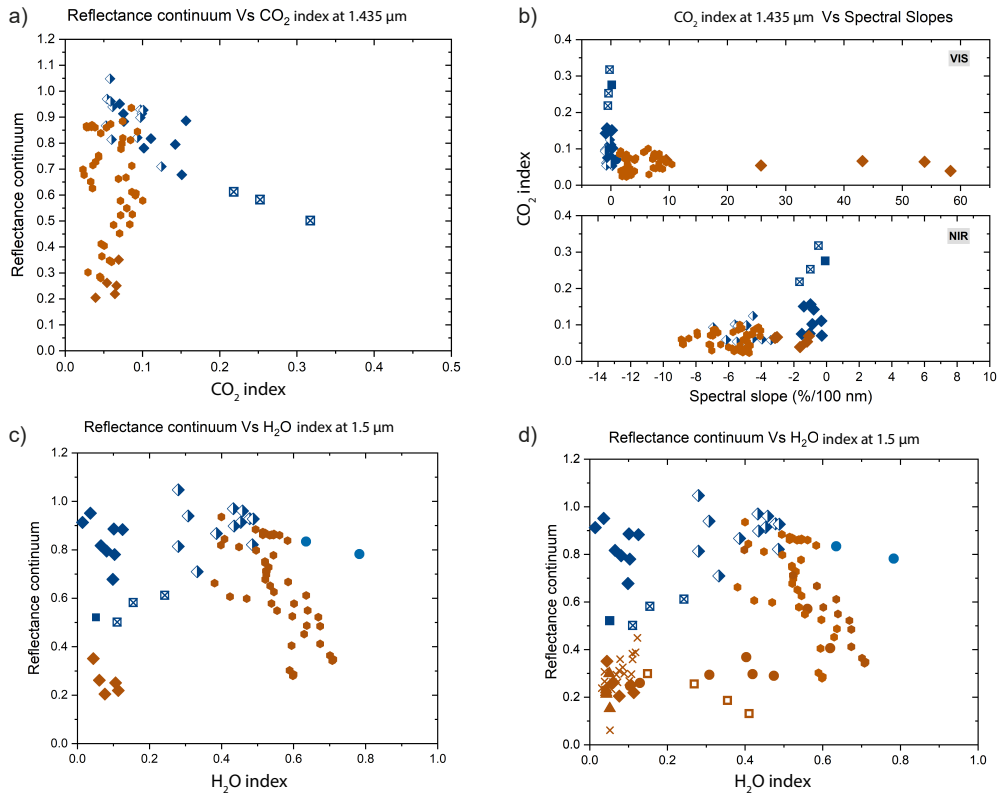


Figure 18: Comparison of spectral criteria between experiments. Addition of H<sub>2</sub>O/dust experiments from [56]. The legend for these plots is provided in Figure 17. Tip: the colours inform about the composition of the samples, and the symbols about their mixing mode/texture a) Reflectance of the continuum v. CO<sub>2</sub> index (1.435 μm). b) CO<sub>2</sub> index (1.435 μm) VS the VIS (top) and NIR (bottom) spectral slopes. c) Reflectance of the continuum VS the H<sub>2</sub>O index (1.5 μm). d) Same as c) with water ice/dust experiments.

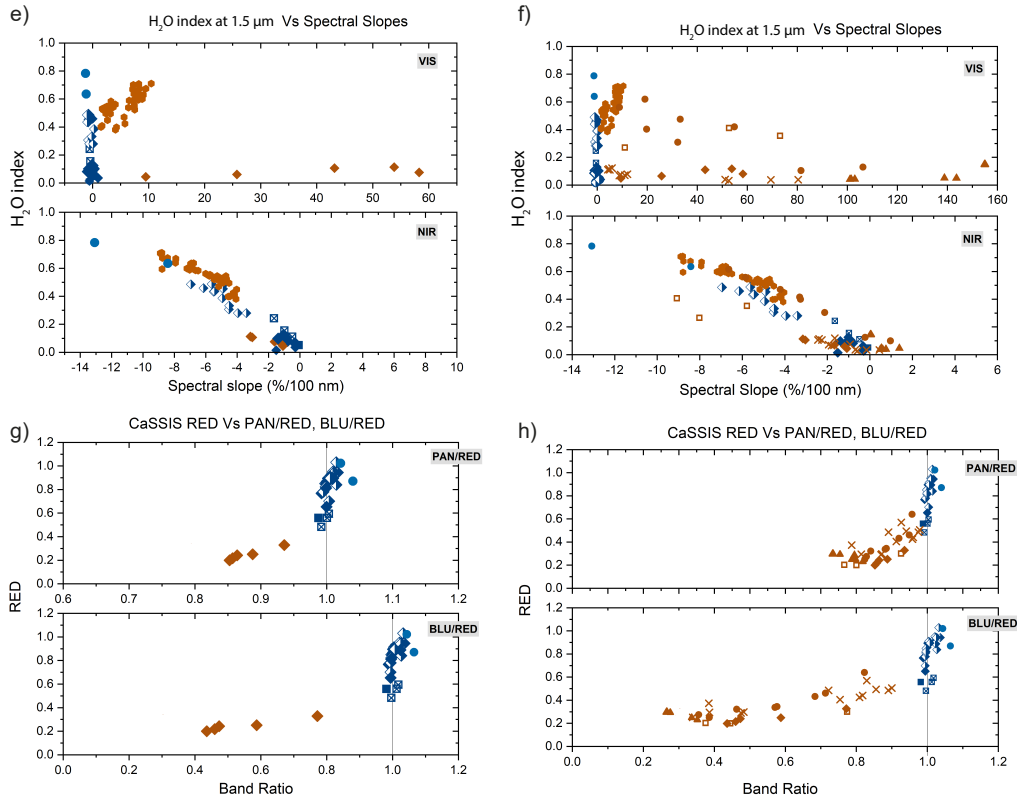


Figure 19: Continuation of Figure 18. Comparison of spectral criteria between experiments. Addition of H<sub>2</sub>O/dust experiments from [56]. The legend for these plots is shown in Figure 17 e) Water index at 1.5 μm versus the VIS (top) and NIR (bottom) spectral slopes. f) Same as e) with water ice/dust experiments. g) Reflectance simulated in the RED filter of CaSSIS versus the PAN/RED (top) and BLU/RED (bottom) ratios. h) Same as g) with the water ice /dust experiments.

932 **4. Discussion**

933 *4.1. Spectro-photometry of pure CO<sub>2</sub>*

934 We have measured the spectra of various size fractions of CO<sub>2</sub> ice in the  
935 spectral range 0.4-2.4  $\mu\text{m}$ . According to Singh and Flanner [19], in a semi-  
936 infinite layer, the size of the CO<sub>2</sub> ice grains affects less the reflectance than  
937 the size of H<sub>2</sub>O ice. In our experiments however, the samples were only 2-  
938 cm thick. While the particles of the CO<sub>2</sub> frost (10-100  $\mu\text{m}$ , see Fig. 2) are  
939 small enough that this particular sample is optically thick (see the discus-  
940 sion of this topic by Hapke [18]), the dark neutral substrate of the sample  
941 holder (constant reflectance of 0.05) certainly affects the continuum level of  
942 the slab and crushed slab samples. Indeed, because of the low absorptiv-  
943 ity of CO<sub>2</sub> in the continuum, photons were able to reach the bottom of the  
944 sample holder. The fact that the samples are not optically thick probably  
945 explains the dependence of continuum reflectance on particle size. But with  
946 the exception of the slab sample (reflectance reduced to 0.5), the effects of  
947 the substrate are relatively minor, with a maximum decrease of reflectance of  
948 0.2 only between the coarsest fraction (400-800  $\mu\text{m}$ ) and the optically thick  
949 snow. This is less than what would be expected from models which predict  
950 a very high transparency of samples made of such large CO<sub>2</sub> particles [19].  
951 The fine-scale texture at the surface of the grains as well as the presence of  
952 interfaces, pores or defects in the interiors of the grains probably increases  
953 the scattering and decreases the penetration compared to idealised smooth  
954 and compact particles. The situation is different at wavelengths where the  
955 absorption is not negligible and the variations of the absorption bands in-  
956 tensity between the different particle size fractions are essentially the results

957 of the change of particle size. However, spectral criteria such as band depth  
958 which consist essentially in a contrast of reflectance between the band and  
959 the continuum will still be affected. Therefore, care must be taken when com-  
960 paring directly these spectra of pure CO<sub>2</sub> ice with Martian spectra but as  
961 the reflectance of the substrate and the thickness of the samples are known,  
962 these spectra remain nevertheless useful to compare to the outputs of models  
963 and simulation.

964 Our spectra of crushed CO<sub>2</sub> ice show a strength of the 2 μm band similar  
965 to the one of the "fractured layer" shown by [48]. We see much more structure  
966 in this band, however, probably because of the higher spectral resolution of  
967 our measurements. Similarly we see strong but narrow absorptions at 1.44  
968 and 1.6 μm, which are not visible in the spectrum of [48]. Our spectrum of  
969 CO<sub>2</sub> frost (10-100 μm) appears very similar to the one labeled as "medium-  
970 grained" in [48] despite the same differences as observed with crushed CO<sub>2</sub>,  
971 again probably because of the different spectral resolution. While there is  
972 no estimate for how large this "medium-grained" frost is, it is larger than  
973 the "fine-grained" CO<sub>2</sub> frost which displays surface texture at the 10-20 μm  
974 scale. This is consistent with the microscope observations of our CO<sub>2</sub> frost  
975 which show large particles of a few tens of μm in diameter.

976 Note that on planetary surfaces as in the laboratory, different grain sizes  
977 can lead to different capacities of atmospheric water frost trapping, which  
978 also indirectly affect the reflectance of the samples.

979 Regardless of the grain size, CO<sub>2</sub> is overall poorly absorptive in the stud-  
980 ied spectral range, with some deep but narrow absorption bands longward of  
981 1.1 μm. In our laboratory spectra, CO<sub>2</sub> presents flat visible spectra; Singh

982 and Flanner [19] modelled, however, a red slope at wavelengths shorter than  
983 0.5  $\mu\text{m}$ , which we have not been able to reproduce, possibly due to the con-  
984 tamination of the surface of the samples by HO frost.

985 Further comparison between modeling results [19] and our experimental  
986 spectra show other differences. In particular, the strength of the  $\text{CO}_2$  ab-  
987 sorption bands in our spectra are consistent with modeled spectra of much  
988 smaller particle size. For instance, our spectrum for the (400-800)  $\mu\text{m}$  size  
989 fraction displays a band depth of about 0.5, similar to the modeled spec-  
990 trum with a particle size of 100  $\mu\text{m}$  in the work of Singh and Flanner [19].  
991 Also surprisingly, the spectrum of our compact slab shows band strengths  
992 much smaller than the modeled spectrum for a particle diameter of 1.5mm  
993 and seems more consistent with a modeled grain size of 500  $\mu\text{m}$  only. These  
994 discrepancies between experimental and modeled results probably originate  
995 from the non-ideal particles produced for the experiments that display ir-  
996 regularities in shape, fine-scales surface texture, internal defects, pores and  
997 joints between grains. All these features of complex real particles combine to  
998 scatter the light at scales much smaller than the actual diameter of spherical  
999 particles assumed in models.

#### 1000 *4.2. $\text{CO}_2$ as a component of a mixture*

1001 As part of a mixture, and because of the flat spectrum of  $\text{CO}_2$  ice,  $\text{CO}_2$   
1002 acts as a reddening material when mixed with a bluer one (e.g., water), and  
1003 as a bluing one when mixed with a redder one (e.g., JSC Mars-1). In this  
1004 regard,  $\text{CO}_2$  ice has similar effects on the reflectance spectra as the early  
1005 stages of water frost deposition. Small amounts of water frost condensed on  
1006 some samples increase the reflectance and flatten the spectral slopes of the

1007 materials underneath, without producing any significant increase in the H<sub>2</sub>O  
1008 indexes [56]. Unfortunately, these similarities complicate the differentiation  
1009 of CO<sub>2</sub> and H<sub>2</sub>O frosts from analysis of visible colours only.

1010 In the first paper of this series, we showed how small amounts of JSC  
1011 Mars-1 were enough to mask water ice when both materials were intimately  
1012 mixed. Here, we observe how small amounts of water ice intimately mixed  
1013 with carbon dioxide ice can mask the CO<sub>2</sub>. This is not a new result as it was  
1014 already shown experimentally by Kieffer [49] (from 0.8 μm) and predicted  
1015 theoretically [72].

1016 We explained in Yoldi et al. [56] that the reflectance of water ice and dust  
1017 intimate mixtures does not increase linearly with the amount of water ice. In-  
1018 stead, the spectra of intimate mixtures are controlled by the most absorptive  
1019 component. JSC Mars-1 is the absorptive material when mixed with H<sub>2</sub>O  
1020 ice, but when we mix H<sub>2</sub>O and CO<sub>2</sub> ices, water ice is the most absorptive  
1021 material. Consequently, the reflectance spectra of intimate mixtures of water  
1022 and carbon dioxide ices are dominated by water ice. This situation reverses  
1023 at wavelengths where water becomes less absorptive than CO<sub>2</sub>. Parameters  
1024 such as grain size or association mode between the materials can balance  
1025 this behaviour of the reflectance spectra [56, 72, 19]. It is still important to  
1026 remember that, when looking at planetary surfaces in the 0.4-2.4 μm spectral  
1027 range, a surface showing a water-like spectrum is not necessarily free of CO<sub>2</sub>,  
1028 in the same way as a surface showing a dust spectrum does not exclude the  
1029 presence of ice [21].

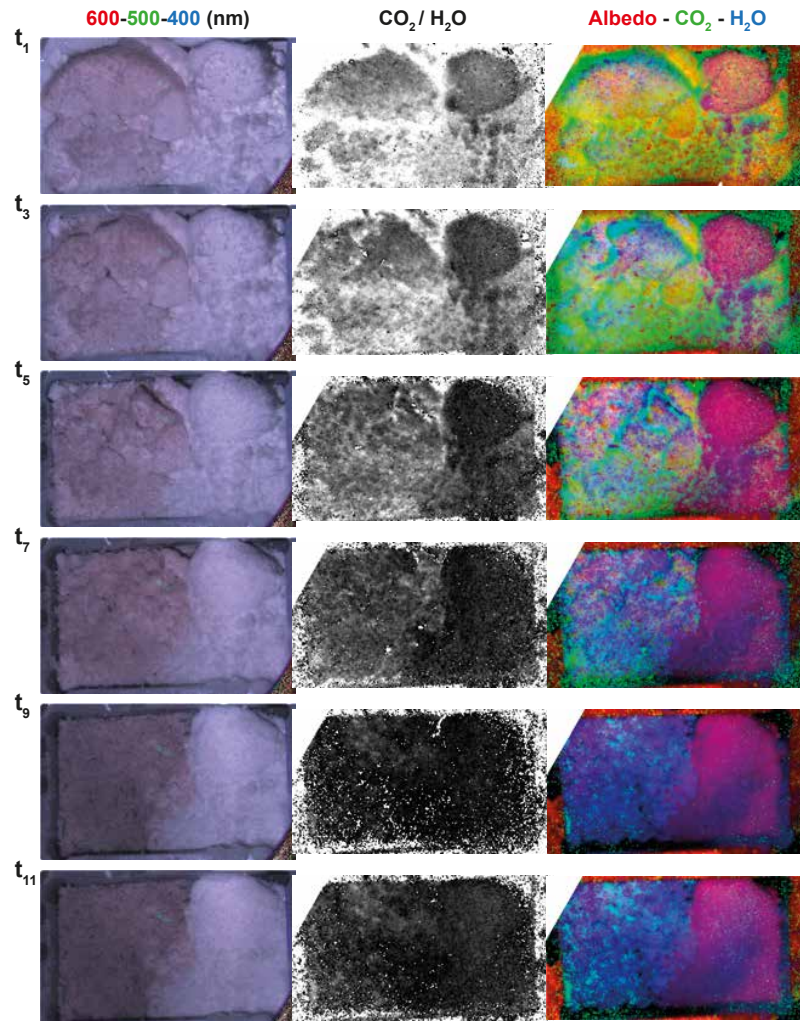


Figure 20: Sublimation series of the ternary mixtures of  $\text{CO}_2$  frost (10-100  $\mu\text{m}$ ), water ice (fine and coarser grained, respectively) and JSC Mars-1. In the left column, we show RGB composites with the signal at 600 nm in the red channel, at 500 nm in the green channel and 400 nm in the blue channel. The column in the middle is a monochromatic image containing the  $\text{CO}_2/\text{H}_2\text{O}$  ratio. The images in this column are stretched from 0.02 to 0.3. The right column shows RGB composites with the continuum reflectance in the red channel, the  $\text{CO}_2$  index in the green channel and the  $\text{H}_2\text{O}$  index in the blue channel. Stretching:  $R(0.318-0.520)$ ,  $G(0.214-0.306)$ ,  $B(0.339-0.575)$ . The rows correspond to the samples at odd times between  $t_1$  and  $t_{11}$ .

1030 *4.3. Ternary mixtures of CO<sub>2</sub>, H<sub>2</sub>O and JSC Mars-1*

1031 Fig 20 shows half of the steps of the sublimation process of ternary mix-  
1032 tures. The complete sequence can be found, in video format, in the sup-  
1033 plementary material. We have produced RGB colour composites with three  
1034 wavelengths (600, 500 and 400 nm) and three spectral parameters (reflectance  
1035 in the continuum, CO<sub>2</sub> signature and H<sub>2</sub>O signature), as well as monochro-  
1036 matic images representing the CO<sub>2</sub>-to-H<sub>2</sub>O ratio.

1037 The images on the left column of Fig 20 provide a good approximation  
1038 to the natural colours of the samples and reveal a different evolution of the  
1039 mixture with fine grained ( $\sim 4.5 \mu\text{m}$ , right) and coarser grained ( $\sim 67 \mu\text{m}$ ,  
1040 left) H<sub>2</sub>O ice. The mixture with fine H<sub>2</sub>O ice particles looks brighter than  
1041 the one with coarser H<sub>2</sub>O ice particles since the scattering by the small par-  
1042 ticles dominates the reflectance throughout the entire sequence. Besides the  
1043 brightness, we observed a distinct evolution of the texture and morphology of  
1044 the samples. In the mixtures with coarser H<sub>2</sub>O ice particles, the compacted  
1045 sample (top of the image, see Fig 2.1.3) broke apart as the volatile compo-  
1046 nents sublimated. At the same time, JSC Mars-1 deposited on top of the  
1047 mixtures, conferring to the sample its characteristic reddish colour. Thus,  
1048 the sample with coarser H<sub>2</sub>O ice appears in  $t_{11}$  as an almost flat deposit of  
1049 JSC Mars-1 mixed with the remaining water ice. The sample with finer H<sub>2</sub>O  
1050 ice, however, seemed to have undergone a process of expansion (this is best  
1051 appreciated on the video): while in  $t_1$  we can still identify the flat surface  
1052 of the compacted sample, from  $t_5$  the sample resembles a porous snowball  
1053 because of the ice filaments it has grown on the surface. The powdered  
1054 sample (below the compacted one) went through the same process, which

1055 progressively softened its surface.

1056 The images on the column in the middle show the evolution of the  
1057  $\text{CO}_2/\text{H}_2\text{O}$  ratio as both sublimated. The pictures have been stretched so  
1058 that black corresponds to  $\text{CO}_2/\text{H}_2\text{O} = 0.02$  and white to  $\text{CO}_2/\text{H}_2\text{O} = 0.3$ .  
1059  $t_1$  already presents the samples bearing fine ice slightly darker than the ones  
1060 with coarse ice. This contrast increases with time so that at  $t_5$  the signa-  
1061 tures of water already dominate the spectrum of the samples where  $\text{H}_2\text{O}$  ice  
1062 is fine grained ( $4.5 \mu\text{m}$ ). The images at  $t_9$  and  $t_{11}$ , although noisy, show a  
1063 little brightening of the samples, related to the increase in the  $\text{CO}_2$  signal  
1064 we measured in Figure 16a. Finally, the RGB composites of spectral crite-  
1065 ria give an overview of the evolution of the albedo and the  $\text{CO}_2$  and  $\text{H}_2\text{O}$   
1066 signatures, represented by the red, green and blue colours, respectively. The  
1067 colours reveal that, from  $t_5$ , a layer of water covers the fine-grained mixtures,  
1068 while green tones are still visible in the coarse-grained ones. In the pictures  
1069 from  $t_7$  and  $t_9$ , we observe that  $\text{CO}_2$  remains preferentially in the creases of  
1070 the material, and in  $t_{11}$ , the strengthening of the signal of  $\text{CO}_2$  appears as  
1071 sparse green dots.

1072 From the information that these images provide, we have reconstructed  
1073 the process of sublimation of the ternary mixtures (Fig 21). In the beginning  
1074 ( $t_1 \sim 160 \text{ K}$ ), the main component subject to sublimation is  $\text{CO}_2$ . As it  
1075 sublimates in the mixture with coarser  $\text{H}_2\text{O}$  ice particles, the surface con-  
1076 centrations of water ice and JSC Mars-1 increase. Around  $t_5$  ( $\sim 195 \text{ K}$ , i.e.,  
1077 the sublimation temperature of  $\text{CO}_2$  ice at 1 atm), all the  $\text{CO}_2$  has subli-  
1078 mated from the surface and the water ice and JSC Mars-1 form a mantle  
1079 that protects the  $\text{CO}_2$  ice underneath from rapid sublimation. In the mix-

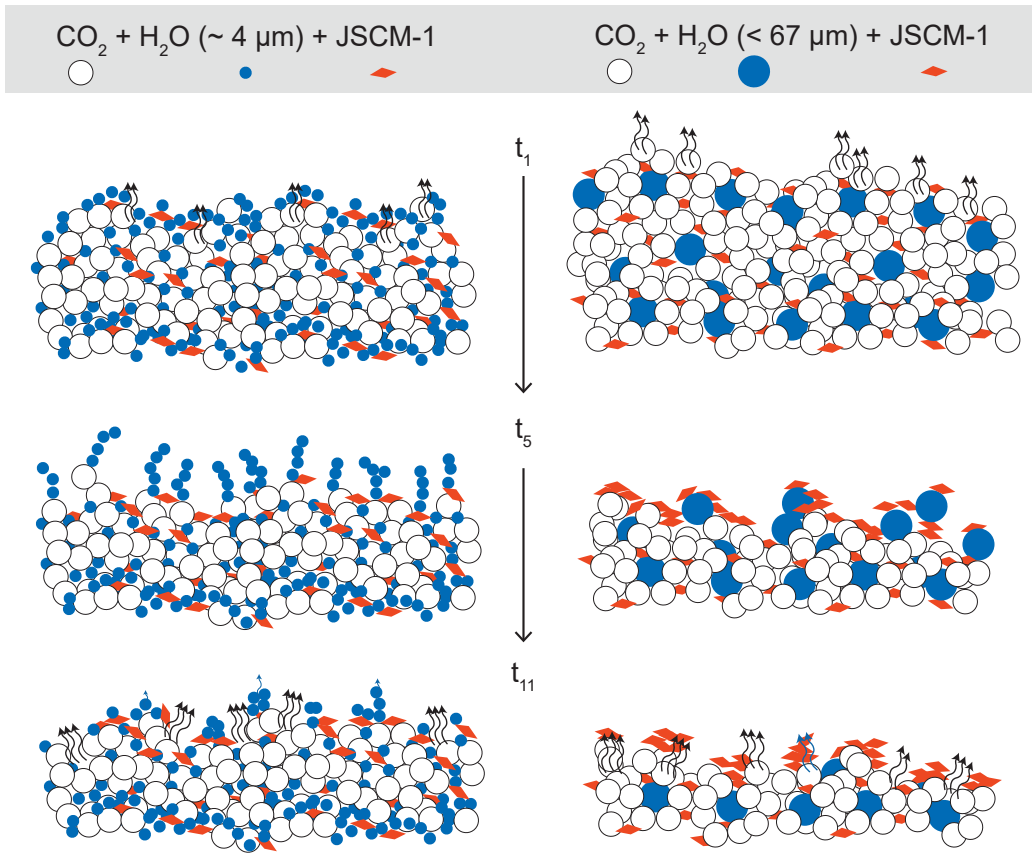


Figure 21: Schematic view of the sublimation processes for ternary mixtures of  $\text{CO}_2$  frost ( $10\text{--}100\ \mu\text{m}$ ),  $\text{H}_2\text{O}$  ice (two different particle sizes) and a finer fraction ( $< 100\ \mu\text{m}$ ) of the JSC Mars-1 regolith simulant. To the left, mixtures with fine  $\text{H}_2\text{O}$  ice particles ( $\sim 4.5\ \mu\text{m}$ ) and to the right with coarser ( $\sim 67\ \mu\text{m}$ ) particles. The three rows represent different times in the sublimation process, increasing from top to bottom and corresponding approximately to  $t_1$ ,  $t_5$  and  $t_{11}$  on Fig 20. As  $\text{CO}_2$  ice (blue particles) sublimates, the JSC Mars-1 dust analogue (red) accumulates at the surface in both cases. The process of sublimation seems to differ depending on the size of the water particles. In the case of coarse ( $\sim 67\ \mu\text{m}$ )  $\text{H}_2\text{O}$  particles, they simply accumulate at the surface and eventually sublimate. The fine ( $\sim 4.5\ \mu\text{m}$ )  $\text{H}_2\text{O}$  ice particles display a different behaviour as they clump together, forming long and thin filaments of water ice which progressively cover most of the surface but are occasionally ejected by the flux of  $\text{CO}_2$  gas produced by the sublimation of the ice.

1080 tures with fine  $\text{H}_2\text{O}$  ice, however, when the grains of  $\text{CO}_2$  sublimate, they  
 1081 carry along the fine grains of water ice. As the  $\text{CO}_2$  gas expands, it cannot

1082 hold the water ice grains any longer, which fall again onto the sample. The  
1083 grains of fine H<sub>2</sub>O ice rearrange then in energetically suitable structures, in  
1084 this case, filaments (t<sub>5</sub>). This step explains the change of texture seen in  
1085 these mixtures, which seemed to grow fluffy. These filaments are effective  
1086 light-scatters; their signal dominates the reflectance and masks the CO<sub>2</sub> ice  
1087 underneath.

1088 As the temperature in our experiment kept increasing, the sublimation  
1089 accelerated. At some point (in our case t<sub>9</sub> or t<sub>11</sub>), the pressure of the subli-  
1090 mating CO<sub>2</sub> gas was strong enough to clear its way out of the sample, piercing  
1091 the sublimation lag and/or breaking the water ice structures. Some of the  
1092 inner CO<sub>2</sub> grains then became visible at the places where this process had  
1093 just occurred.

1094 This sequence of differential sublimation explains why the CO<sub>2</sub> index  
1095 does not drop linearly with sublimation (see Fig 16). Instead, the signal  
1096 first drops, levels out and then increases for mixtures with fine grained H<sub>2</sub>O  
1097 ice and oscillates in the beginning to then drop and again rise for mixtures  
1098 with coarser H<sub>2</sub>O ice. It also explains why the H<sub>2</sub>O signal does not increase  
1099 linearly, but initially increases to eventually level out (fine H<sub>2</sub>O) or slow  
1100 down (coarser H<sub>2</sub>O). The growth of the CO<sub>2</sub> signal once it seemed to be  
1101 gone could also be explained by the release of previously adsorbed CO<sub>2</sub> on  
1102 JSC Mars-1 microparticles or possibly by the decomposition of CO<sub>2</sub> clathrate  
1103 hydrates (Vincent Chevrier, personal communication). Presumably, how this  
1104 sublimation sequence develops depends on factors such as the CO<sub>2</sub>-to-H<sub>2</sub>O  
1105 ratio, the grain size of the refractory material or the association mode of the  
1106 materials (as seen in Poch et al. [73]).

1107 Finally, these experiments provide experimental support for the hypoth-  
1108 esis formulated in Appéré et al. [42] and Pommerol et al. [45] regarding the  
1109 disappearance and subsequent return of the spectral signal of CO<sub>2</sub>. A thin  
1110 mantle of fine water frost masks the signature of CO<sub>2</sub>, which reappears as  
1111 the water frost layer disrupts with the increase of temperature.

#### 1112 4.4. Use of spectral parameters to identify mixtures

1113 To identify CO<sub>2</sub> ice, the first thing to look for is its absorption feature  
1114 at 1.435 μm. As we have repeatedly noted, the detection of a CO<sub>2</sub> signature  
1115 evinces the presence of that component, but the lack of a signature does  
1116 not guarantee the absence of CO<sub>2</sub> since it could be mixed intimately with  
1117 other components (e.g., water ice) and masked. We can also get a hint about  
1118 the presence of CO<sub>2</sub> ice by looking at the continuum reflectance against the  
1119 water index at 1.5 μm (Fig 18d); CO<sub>2</sub>-bearing experiments stand out with  
1120 high reflectance at weak water indices.

1121 *CO<sub>2</sub> Vs. CO<sub>2</sub> + dust.* To identify dust in the mixtures, looking at the CaSSIS  
1122 colours provide a direct answer. Indeed, every sample containing JSC Mars-  
1123 1 falls under BLU/RED ratios of 0.9, while pure ice samples fall around  
1124 BLU/RED ratios of 1.0. Alternatively, comparing the visible spectral slope  
1125 to either the water or the carbon dioxide indexes is a good strategy to identify  
1126 most of the JSC Mars-1 - bearing samples.

1127 *CO<sub>2</sub> Vs. CO<sub>2</sub> + H<sub>2</sub>O.* In order to identify water ice, we look at the H<sub>2</sub>O  
1128 index; for example, by comparing the visible spectral slope against the water  
1129 index. Comparing first the water index to the visible spectral slope and then  
1130 to the NIR spectral slope allows us first to identify pure ice samples, and then

1131 to identify whether the samples are made of pure water ice, intimate mixtures  
1132 of carbon dioxide and water ices or pure carbon dioxide. Looking at the CO<sub>2</sub>  
1133 index versus the NIR spectral slope also allows us to differentiate between  
1134 intimate mixtures of water and carbon dioxide ices, pure CO<sub>2</sub> samples and  
1135 slabs.

1136 *Atmospheric frost.* In our previous publication, we pointed out the compar-  
1137 ison of the H<sub>2</sub>O index and the visible slope as being useful to identify water  
1138 frost [56]. When we incorporate the CO<sub>2</sub> experiments, this identification be-  
1139 comes more difficult, since CO<sub>2</sub> and small condensates of water frost share  
1140 the same reflectance characteristics: they are bright, they tend to flatten the  
1141 spectral slope of the substrate they are mixed with, and they do not alter the  
1142 absorption bands of water. Therefore, it is hard to tell whether the intimate  
1143 mixtures with JSC Mars-1 have trapped water frost by looking at Fig 19f  
1144 (VIS). We have to look as well at the near-infrared, where water and carbon  
1145 dioxide behave differently, water being bluer than carbon dioxide. In Fig 19f  
1146 (NIR) we observe that two of the symbols for CO<sub>2</sub> and JSC Mars-1 intimate  
1147 mixtures in the graph at the bottom follow the trend drawn by the JSCM-  
1148 1/water frost experiments instead of remaining with the pure CO<sub>2</sub> or pure  
1149 JSC Mars-1 samples. The corresponding experiments have indeed trapped  
1150 water frost.

#### 1151 4.5. *Limitations of the measurements.*

1152 As mentioned in Section 2, it is challenging to achieve homogeneous inti-  
1153 mate mixtures in which the end members are present in extreme ratios (i.e.,  
1154 10 wt% - 90 wt% instead of 50 wt%- 50 wt%). The task becomes even more

1155 challenging when both components have the same colour since we cannot  
1156 assess visually how well they mix. The measured reflectance showed that  
1157 we succeeded in obtaining different CO<sub>2</sub>-to-H<sub>2</sub>O ratios. However, due to the  
1158 formation of agglomerates, the samples were not as homogeneous as desired  
1159 (see for example Fig 4a). Kieffer [49] already noted the difficulty of linking  
1160 the reflectance spectra to the composition of his samples, due to textural  
1161 effects. In the same way, we are not able to identify the mixtures displaying  
1162 more water ice from their reflectance in the visible. In the near-infrared,  
1163 however, the presence of the absorption bands of water allows us to notice  
1164 the increasing amount of water ice within the samples.

1165     Because of the fast sintering of CO<sub>2</sub> ice grains, fine granular surfaces  
1166 are hard to achieve [74]. Further laboratory work is needed to achieve CO<sub>2</sub>  
1167 samples free from agglomerates, to first study their reflectance with smooth  
1168 surfaces, and then understand the nature of agglomerates as well as their  
1169 effect on the reflectance. We need to understand, for instance, whether we  
1170 are creating these agglomerates by manipulating the samples, whether they  
1171 only form at atmospheric pressures or whether small granular sliding at the  
1172 surface of ice is enough to create them.

## 1173 5. Conclusions

1174 We have reported on the reflectance measurements carried out at LOSSy  
1175 on analogues for the surface of Mars containing H<sub>2</sub>O and CO<sub>2</sub> ice (at at-  
1176 mospheric pressure). We have measured the reflectance of pure CO<sub>2</sub> frost,  
1177 ice grains and slabs, and we have mixed CO<sub>2</sub> with water ice (intimate mix-  
1178 ture and as frost contamination) and/or JSC Mars-1. We have monitored  
1179 the reflectance of a ternary mixture of CO<sub>2</sub>, H<sub>2</sub>O and JSC Mars-1 as the  
1180 volatile components sublimated. We summarise below the general trends  
1181 we've observed:

- 1182 • The size of particles of CO<sub>2</sub> plays a key role in the reflectance in var-  
1183 ious ways. i) Large particles transport photons deep in the medium,  
1184 while small particles scatter light more efficiently, masking the mate-  
1185 rial underneath the ice ii) Small particle sizes trap more of atmospheric  
1186 water.
- 1187 • The reflectance in the visible of the mixtures with granulated CO<sub>2</sub> is  
1188 dominated by effects of the texture rather than the composition itself.  
1189 In the near-infrared, however, the composition drives the reflectance.
- 1190 • As a part of a mixture, CO<sub>2</sub> is easily masked by more absorbent com-  
1191 ponents due to its weak absorptivity. The materials tested here (water  
1192 ice and JSC Mars-1) being much more absorptive than CO<sub>2</sub>, masked  
1193 the characteristic absorption features of CO<sub>2</sub> out of proportion to their  
1194 presence.
- 1195 • The evolution of the reflectance of our ternary mixtures as tempera-  
1196 ture increased was controlled by the size of the particles of water ice,

1197 even if present only at 3 wt%. The sublimation of CO<sub>2</sub> caused the JSC  
1198 Mars-1 and coarse-grained water ice to settle down and cover the ice  
1199 underneath. The sublimation of CO<sub>2</sub> also caused the fine-grained water  
1200 ice to form highly-scattering H<sub>2</sub>O frost filaments over the CO<sub>2</sub> ice un-  
1201 derneath, compatible with the observations of the northern, seasonal,  
1202 polar cap of Mars by Appéré et al. [42] and Pommerol et al. [45].

- 1203 • We have compared many spectral parameters in the visible and near-  
1204 infrared spectral ranges to make our data useful for a wide range of  
1205 instruments measuring the reflectance of the Martian surface.
  
- 1206 • If we want to know about the grain size of the CO<sub>2</sub> ice, it is useful to  
1207 compare the reflectance in the continuum versus the CO<sub>2</sub> index. To  
1208 study the colour of the sample is useful to spot dust within the ice  
1209 samples: CaSSIS colours or comparing the visible spectral slope to the  
1210 water or carbon dioxide indexes will reveal the presence of dust on a  
1211 sample. If we compare the water index first to the visible and then to  
1212 the NIR spectral slope, we can identify if pure ice samples are made  
1213 only of water ice or carbon dioxide ice or if they are a mix of both.
  
- 1214 • It is hard to identify water frost over CO<sub>2</sub> ice by looking at the re-  
1215 flectance spectra of the sample. However, the comparison of the water  
1216 index versus the visible and NIR spectral slopes is a good indicator of  
1217 the presence of water frost over surfaces.
  
- 1218 • Comparing visible and NIR slopes can be a way of identifying CO<sub>2</sub> ice  
1219 for instruments that cannot resolve absorption features.

1220 The methods that we have proposed in these two papers (see Yoldi et al.  
1221 [56]) provide a useful tool to fully exploit reflectance data. Because of the  
1222 variety of spectral criteria and ranges used, these tools can be used with the  
1223 data of many instruments that measure or have measured the reflectance of  
1224 the surface of Mars (i.e., OMEGA, CRISM, HRSC, HiRISE and CaSSIS).  
1225 They are also useful to calibrate reflectance models.

1226 **Data availability** All the reflectance spectra presented here are avail-  
1227 able on the Bern icY Planetary Analogues Solid Spectroscopy (BYPASS)  
1228 database, hosted on the Solid Spectroscopy Hosting Architecture of Databases  
1229 and Expertise (SSHADE) . *Direct DOI link to the data will be provided here*  
1230 *upon acceptance.*

1231 **Acknowledgements** This work has been developed in the framework of  
1232 the National Center for Competence in Research PlanetS funded by the Swiss  
1233 National Science Foundation (SNSF). The authors want to thank Vincent  
1234 Chevrier, Aditya Khuller and an anonymous reviewer for their valuable and  
1235 constructive comments on this article.

- 1236 [1] G. Filacchione, A. Raponi, F. Capaccioni, M. Ciarniello, F. Tosi, M. T.  
1237 Capria, M. C. De Sanctis, A. Migliorini, G. Piccioni, P. Cerroni, M. A.  
1238 Barucci, S. Fornasier, B. Schmitt, E. Quirico, S. Erard, D. Bockelee-  
1239 Morvan, C. Leyrat, G. Arnold, V. Mennella, E. Ammannito, G. Bel-  
1240 lucci, J. Benkhoff, J. P. Bibring, A. Blanco, M. I. Blecka, R. Carl-  
1241 son, U. Carsenty, L. Colangeli, M. Combes, M. Combi, J. Crovisier,  
1242 P. Drossart, T. Encrenaz, C. Federico, U. Fink, S. Fonti, M. Fulchignoni,  
1243 W.-H. Ip, P. Irwin, R. Jaumann, E. Kuehrt, Y. Langevin, G. Magni,  
1244 T. McCord, L. Moroz, S. Mottola, E. Palomba, U. Schade, K. Stephan,  
1245 F. Taylor, D. Tiphene, G. P. Tozzi, P. Beck, N. Biver, L. Bonal, J.-P.  
1246 Combe, D. Despan, E. Flamini, M. Formisano, A. Frigeri, D. Grassi,  
1247 M. S. Gudipati, D. Kappel, A. Longobardo, F. Mancarella, K. Markus,  
1248 F. Merlin, R. Orosei, G. Rinaldi, M. Cartacci, A. Cicchetti, Y. Hello,  
1249 F. Henry, S. Jacquino, J. M. Reess, R. Noschese, R. Politi, G. Pe-  
1250 ter, Seasonal exposure of carbon dioxide ice on the nucleus of comet  
1251 67p/churyumov-gerasimenko, *Science* 354 (2016) 1563–1566.
- 1252 [2] D. P. Cruikshank, R. T. L., O. T. C., G. T. R., d. B. C., S. B., B. R. H.,  
1253 B. M. J., Ices on the surface of triton, *Science* 261 (1993) 742745.
- 1254 [3] P. R. Mahaffy, C. R. Webster, S. K. Atreya, H. Franz, M. Wong, P. G.  
1255 Conrad, D. Harpold, J. J. Jones, L. A. Leshin, H. Manning, T. Owen,  
1256 R. O. Pepin, S. Squyres, M. Trainer, , Abundance and isotopic com-  
1257 position of gases in the martian atmosphere from the curiosity rover,  
1258 *Science* 341 (2013) 263–266.
- 1259 [4] J. B. Pollack, R. M. Haberle, J. Schaeffer, H. Lee, Simulations of the

- 1260        general circulation of the martian atmosphere: 1. polar processes, Jour-  
1261        nal of Geophysical Research: Solid Earth 95 (1990) 1447–1473.
- 1262    [5] F. Hourdin, F. Forget, O. Talagrand, The sensitivity of the martian  
1263        surface pressure and atmospheric mass budget to various parameters:  
1264        A comparison between numerical simulations and viking observations,  
1265        Journal of Geophysical Research: Planets 100 (1995) 5501–5523.
- 1266    [6] P. B. James, H. H. Kieffer, D. A. Paige, The seasonal cycle of carbon  
1267        dioxide on mars, Mars (1992) 934–968.
- 1268    [7] B. M. Jakosky, The seasonal cycle of water on mars, Space science  
1269        reviews 41 (1985) 131–200.
- 1270    [8] R. Kahn, S. Lee, T. Martin, R. Zurek, The martian dust cycle, in:  
1271        Bulletin of the American Astronomical Society, volume 22, p. 1076.
- 1272    [9] S. Piqueux, A. Kleinbhl, P. O. Hayne, N. G. Heavens, D. M. Kass,  
1273        D. J. McCleese, J. T. Schofield, J. H. Shirley, Discovery of a widespread  
1274        low-latitude diurnal co2 frost cycle on mars, Journal of Geophysical  
1275        Research: Planets 121 (2016) 1174–1189.
- 1276    [10] G. Neugebauer, G. Mnch, H. Kieffer, J. Chase, S. C., E. Miner, Mariner  
1277        1969 infrared radiometer results: Temperatures and thermal properties  
1278        of the martian surface, Astronomical Journal 76 (1971) 719.
- 1279    [11] R. B. Leighton, B. C. Murray, Behavior of carbon dioxide and other  
1280        volatiles on mars, Science 153 (1966) 136–144.

- 1281 [12] S. G. Warren, Optical constants of ice from the ultraviolet to the mi-  
1282 crowave, 23 (1984) 1206–1225.
- 1283 [13] S. G. Warren, Optical constants of carbon dioxide ice, 25 (1986) 2650–  
1284 2674.
- 1285 [14] Hansen, The infrared absorption spectrum of carbon dioxide ice from  
1286 1.8 to 333  $\mu\text{m}$ , Journal of Geophysical Research: Planets 102 (1997)  
1287 21569–21587.
- 1288 [15] Hansen, Ultraviolet to nearinfrared absorption spectrum of carbon diox-  
1289 ide ice from 0.174 to 1.8  $\mu\text{m}$ , Journal of Geophysical Research: Planets  
1290 110 (2005).
- 1291 [16] C. F. Bohren, B. R. Barkstrom, Theory of the optical properties of  
1292 snow, 79 (1974) 4527–4535.
- 1293 [17] W. J. Wiscombe, S. G. Warren, A Model for the Spectral Albedo of  
1294 Snow. I: Pure Snow., Journal of Atmospheric Sciences 37 (1980) 2712–  
1295 2733.
- 1296 [18] B. Hapke, Theory of reflectance and emittance spectroscopy, 1993.
- 1297 [19] D. Singh, M. G. Flanner, An improved carbon dioxide snow spectral  
1298 albedo model: Application to martian conditions, Journal of Geophysi-  
1299 cal Research: Planets 121 (2016) 2037–2054. 2016JE005040.
- 1300 [20] A. R. Khuller, P. R. Christensen, S. G. Warren, Spectral Albedo of  
1301 Dusty Martian H<sub>2</sub>O Snow and Ice, Journal of Geophysical Research  
1302 (Planets) 126 (2021) e06910.

- 1303 [21] Z. Yoldi, A. Pommerol, B. Jost, O. Poch, J. Gouman, N. Thomas, Vis-  
1304 nir reflectance of water ice/regolith analogue mixtures and implications  
1305 for the detectability of ice mixed within planetary regoliths, *Geophysical*  
1306 *Research Letters* 42 (2015) 6205–6212. 2015GL064780.
- 1307 [22] P. C. Thomas, M. C. Malin, P. B. James, B. A. Cantor, R. M. E.  
1308 Williams, P. Gierasch, South polar residual cap of Mars: Features,  
1309 stratigraphy, and changes, 174 (2005) 535–559.
- 1310 [23] T. N. Titus, H. H. Kieffer, P. R. Christensen, Exposed water ice discov-  
1311 ered near the south pole of mars, *Science* 299 (2003) 1048–1051.
- 1312 [24] J. J. Plaut, G. Picardi, A. Safaeinili, A. B. Ivanov, S. M. Milkovich,  
1313 A. Cicchetti, W. Kofman, J. Mouginot, W. M. Farrell, R. J. Phillips,  
1314 S. M. Clifford, A. Frigeri, R. Orosei, C. Federico, I. P. Williams, D. A.  
1315 Gurnett, E. Nielsen, T. Hagfors, E. Heggy, E. R. Stofan, D. Plettemeier,  
1316 T. R. Watters, C. J. Leuschen, P. Edenhofer, Subsurface Radar Sound-  
1317 ing of the South Polar Layered Deposits of Mars, *Science* 316 (2007)  
1318 92.
- 1319 [25] C. J. Bierson, R. J. Phillips, I. B. Smith, S. E. Wood, N. E. Putzig,  
1320 D. Nunes, S. Byrne, Stratigraphy and evolution of the buried CO<sub>2</sub>  
1321 deposit in the Martian south polar cap, 43 (2016) 4172–4179.
- 1322 [26] J.-P. Bibring, Y. Langevin, F. Poulet, A. Gendrin, B. Gondet,  
1323 M. Berthé, A. Soufflot, P. Drossart, M. Combes, G. Bellucci, V. Moroz,  
1324 N. Mangold, B. Schmitt, OMEGA Team, S. Erard, O. Forni, N. Man-  
1325 aud, G. Poulleau, T. Encrenaz, T. Fouchet, R. Melchiorri, F. Altieri,

- 1326 V. Formisano, G. Bonello, S. Fonti, F. Capaccioni, P. Cerroni, A. Cora-  
1327 dini, V. Kottsov, N. Ignatiev, D. Titov, L. Zasova, P. Pinet, C. Sotin,  
1328 E. Hauber, H. Hoffman, R. Jaumann, U. Keller, R. Arvidson, J. Mus-  
1329 tard, T. Duxbury, F. Forget, Perennial water ice identified in the south  
1330 polar cap of Mars, 428 (2004) 627–630.
- 1331 [27] W. M. Calvin, T. Z. Martin, Spatial variability in the seasonal south  
1332 polar cap of mars, *Journal of Geophysical Research: Planets* 99 (1994)  
1333 21143–21152.
- 1334 [28] H. H. Kieffer, T. N. Titus, K. F. Mullins, P. R. Christensen, Mars  
1335 south polar spring and summer behavior observed by tes: Seasonal cap  
1336 evolution controlled by frost grain size, *Journal of Geophysical Research:*  
1337 *Planets* 105 (2000) 9653–9699.
- 1338 [29] H. H. Kieffer, Cold jets in the Martian polar caps, *Journal of Geophysical*  
1339 *Research (Planets)* 112 (2007) E08005.
- 1340 [30] Y. Langevin, J.-P. Bibring, F. Montmessin, F. Forget, M. Vincendon,  
1341 S. Douté, F. Poulet, B. Gondet, Observations of the south seasonal cap  
1342 of mars during recession in 20042006 by the omega visible/near-infrared  
1343 imaging spectrometer on board mars express, *Journal of Geophysical*  
1344 *Research: Planets* 112 (2007) n/a–n/a. E08S12.
- 1345 [31] S. Murchie, R. Arvidson, P. Bedini, K. Beisser, J. P. Bibring, J. Bishop,  
1346 J. Boldt, P. Cavender, T. Choo, R. T. Clancy, E. H. Darlington, D. Des  
1347 Marais, R. Espiritu, D. Fort, R. Green, E. Guinness, J. Hayes, C. Hash,  
1348 K. Heffernan, J. Hemmler, G. Heyler, D. Humm, J. Hutcheson, N. Izen-

- 1349 berg, R. Lee, J. Lees, D. Lohr, E. Malaret, T. Martin, J. A. McGovern,  
1350 P. McGuire, R. Morris, J. Mustard, S. Pelkey, E. Rhodes, M. Robinson,  
1351 T. Roush, E. Schaefer, G. Seagrave, F. Seelos, P. Silverglate, S. Slavney,  
1352 M. Smith, W. J. Shyong, K. Strohbahn, H. Taylor, P. Thompson,  
1353 B. Tossman, M. Wirzburger, M. Wolff, Compact Reconnaissance Imag-  
1354 ing Spectrometer for Mars (CRISM) on Mars Reconnaissance Orbiter  
1355 (MRO), *Journal of Geophysical Research (Planets)* 112 (2007) E05S03.
- 1356 [32] J. F. Bell, M. J. Wolff, M. C. Malin, W. M. Calvin, B. A. Cantor,  
1357 M. A. Caplinger, R. T. Clancy, K. S. Edgett, L. J. Edwards, J. Fahle,  
1358 F. Ghaemi, R. M. Haberle, A. Hale, P. B. James, S. W. Lee, T. Mc-  
1359 Connochie, E. Noe Dobrea, M. A. Ravine, D. Schaeffer, K. D. Supul-  
1360 ver, P. C. Thomas, Mars Reconnaissance Orbiter Mars Color Imager  
1361 (MARCI): Instrument description, calibration, and performance, *Jour-  
1362 nal of Geophysical Research (Planets)* 114 (2009) E08S92.
- 1363 [33] A. J. Brown, W. M. Calvin, P. C. McGuire, S. L. Murchie, Compact  
1364 reconnaissance imaging spectrometer for mars (crism) south polar map-  
1365 ping: First mars year of observations, *Journal of Geophysical Research:  
1366 Planets* 115 (2010).
- 1367 [34] A. S. McEwen, E. M. Eliason, J. W. Bergstrom, N. T. Bridges, C. J.  
1368 Hansen, W. A. Delamere, J. A. Grant, V. C. Gulick, K. E. Herkenhoff,  
1369 L. Keszthelyi, R. L. Kirk, M. T. Mellon, S. W. Squyres, N. Thomas,  
1370 C. M. Weitz, Mars Reconnaissance Orbiter's High Resolution Imaging  
1371 Science Experiment (HiRISE), *Journal of Geophysical Research (Plan-  
1372 ets)* 112 (2007) E05S02.

- 1373 [35] A. Pommerol, G. Portyankina, N. Thomas, K.-M. Aye, C. J. Hansen,  
1374 M. Vincendon, Y. Langevin, Evolution of south seasonal cap during  
1375 martian spring: Insights from high-resolution observations by hirise and  
1376 crism on mars reconnaissance orbiter, *Journal of Geophysical Research:*  
1377 *Planets* 116 (2011) n/a–n/a. E08007.
- 1378 [36] A. J. Brown, S. Piqueux, T. N. Titus, Interannual observations and  
1379 quantification of summertime h<sub>2</sub>o ice deposition on the martian co<sub>2</sub> ice  
1380 south polar cap, *Earth and Planetary Science Letters* 406 (2014) 102–  
1381 109.
- 1382 [37] P. R. Christensen, B. M. Jakosky, H. H. Kieffer, M. C. Malin, J. Mc-  
1383 Sween, Harry Y., K. Neelson, G. L. Mehall, S. H. Silverman, S. Ferry,  
1384 M. Caplinger, M. Ravine, The Thermal Emission Imaging System  
1385 (THEMIS) for the Mars 2001 Odyssey Mission, 110 (2004) 85–130.
- 1386 [38] P. R. Christensen, J. L. Bandfield, V. E. Hamilton, S. W. Ruff, H. H.  
1387 Kieffer, T. N. Titus, M. C. Malin, R. V. Morris, M. D. Lane, R. L. Clark,  
1388 B. M. Jakosky, M. T. Mellon, J. C. Pearl, B. J. Conrath, M. D. Smith,  
1389 R. T. Clancy, R. O. Kuzmin, T. Roush, G. L. Mehall, N. Gorelick,  
1390 K. Bender, K. Murray, S. Dason, E. Greene, S. Silverman, M. Green-  
1391 field, Mars Global Surveyor Thermal Emission Spectrometer experi-  
1392 ment: Investigation description and surface science results, 106 (2001)  
1393 23823–23872.
- 1394 [39] K. L. Wagstaff, T. N. Titus, A. B. Ivanov, R. Castaño, J. L. Band-  
1395 field, Observations of the north polar water ice annulus on Mars using  
1396 THEMIS and TES, 56 (2008) 256–265.

- 1397 [40] H. Houben, R. M. Haberle, R. E. Young, A. P. Zent, Modeling the  
1398 Martian seasonal water cycle, 102 (1997) 9069–9084.
- 1399 [41] Y. Langevin, F. Poulet, J.-P. Bibring, B. Schmitt, S. Douté, B. Gondet,  
1400 Summer evolution of the north polar cap of mars as observed by  
1401 omega/mars express, Science 307 (2005) 1581–1584.
- 1402 [42] T. Appéré, B. Schmitt, Y. Langevin, S. Douté, A. Pommerol, F. Forget,  
1403 A. Spiga, B. Gondet, J.-P. Bibring, Winter and spring evolution of  
1404 northern seasonal deposits on mars from omega on mars express, Journal  
1405 of Geophysical Research: Planets 116 (2011) n/a–n/a. E05001.
- 1406 [43] C. Hansen, S. Byrne, G. Portyankina, M. Bourke, C. Dundas,  
1407 A. McEwen, M. Mellon, A. Pommerol, N. Thomas, Observations of  
1408 the northern seasonal polar cap on mars: I. spring sublimation activity  
1409 and processes, Icarus 225 (2013) 881 – 897. Mars Polar Science V.
- 1410 [44] G. Portyankina, A. Pommerol, K.-M. Aye, C. J. Hansen, N. Thomas,  
1411 Observations of the northern seasonal polar cap on mars ii: Hirise pho-  
1412 tometric analysis of evolution of northern polar dunes in spring, Icarus  
1413 225 (2013) 898 – 910. Mars Polar Science V.
- 1414 [45] A. Pommerol, T. Appr, G. Portyankina, K.-M. Aye, N. Thomas,  
1415 C. Hansen, Observations of the northern seasonal polar cap on mars  
1416 iii: Crism/hirise observations of spring sublimation, Icarus 225 (2013)  
1417 911 – 922. Mars Polar Science V.
- 1418 [46] E. Quirico, B. Schmitt, Near-infrared spectroscopy of simple hydrocar-

- 1419       bons and carbon oxides diluted in solid  $n_2$  and as pure ices: Implications  
1420       for triton and pluto, *Icarus* 127 (1997) 354 – 378.
- 1421 [47] K. I. Öberg, H. J. Fraser, A. C. A. Boogert, S. E. Bisschop, G. W. Fuchs,  
1422       E. F. van Dishoeck, H. Linnartz, Effects of  $CO_2$  on  $H_2O$  band profiles  
1423       and band strengths in mixed  $H_2O:CO_2$  ices, 462 (2007) 1187–1198.
- 1424 [48] H. H. Kieffer, Near infrared spectral reflectance of simulated Martian  
1425       frosts, Ph.D. thesis, California Institute of Technology, United States,  
1426       1968.
- 1427 [49] H. Kieffer, Spectral reflectance of  $CO_2$ - $H_2O$  frosts, *Journal of Geophysical*  
1428       *Research* 75 (1970) 501–509.
- 1429 [50] M. P. Bernstein, D. P. Cruikshank, S. A. Sandford, Near-infrared labo-  
1430       ratory spectra of solid  $H_2O/CO_2$  and  $CH_3OH/CO_2$  ice mixtures, *Icarus* 179  
1431       (2005) 527–534.
- 1432 [51] A. Oancea, O. Grasset, E. Le Menn, O. Bollengier, L. Bezacier, S. Le  
1433       Mouélic, G. Tobie, Laboratory infrared reflection spectrum of carbon  
1434       dioxide clathrate hydrates for astrophysical remote sensing applications,  
1435       221 (2012) 900–910.
- 1436 [52] F. Grisolle, T. Appr, B. Schmitt, P. Beck, O. Brissaud, S. Dout, In-  
1437       fluence of condensing water frost on the near-ir spectrum of  $CO_2$  snow  
1438       (2011).
- 1439 [53] S. Philippe, B. Schmitt, P. Beck, O. Brissaud, Sublimation of  $CO_2$  ice  
1440       with  $H_2O$  ice contamination: analogy with the sublimation of mars sea-  
1441       sonal caps (2015).

- 1442 [54] B. Schmitt, S. Philippe, P. Beck, O. Brissaud, Sublimation at grain  
1443 boundaries of polycrystalline  $\text{CO}_2$  slab ice: the clue to the strong spring  
1444 albedo increase of the martian seasonal polar caps (2020).
- 1445 [55] G. Portyankina, J. Merrison, J. Iversen, Z. Yoldi, C. Hansen, K.-M. Aye,  
1446 A. Pommerol, N. Thomas, Laboratory investigations of the physical  
1447 state of  $\text{CO}_2$  ice in a simulated martian environment, *Icarus* 322 (2019)  
1448 210 – 220.
- 1449 [56] Z. Yoldi, A. Pommerol, O. Poch, N. Thomas, Reflectance study of ice  
1450 and mars soil simulant associations i.  $\text{H}_2\text{O}$  ice, *Icarus* (2020) 114169.
- 1451 [57] A. Pommerol, B. Jost, O. Poch, Z. Yoldi, Y. Brouet, A. Gracia-Berná,  
1452 R. Cerubini, A. Galli, P. Wurz, B. Gundlach, J. Blum, N. Carrasco,  
1453 C. Szopa, N. Thomas, Experimenting with mixtures of water ice and  
1454 dust as analogues for icy planetary material, *Space Science Reviews* 215  
1455 (2019) 37.
- 1456 [58] F. Forget, G. B. Hansen, J. B. Pollack, Low brightness temperatures of  
1457 martian polar caps:  $\text{CO}_2$  clouds or low surface emissivity?, *Journal of*  
1458 *Geophysical Research: Planets* 100 (1995) 21219–21234.
- 1459 [59] H. H. Kieffer, P. R. Christensen, T. N. Titus,  $\text{CO}_2$  jets formed by sub-  
1460 limation beneath translucent slab ice in mars' seasonal south polar ice  
1461 cap, *Nature* 442 (2006).
- 1462 [60] Y. Brouet, Contribution à la détermination de la permittivité des noy-  
1463 aux cométaires et des astéroïdes, 2013.

- 1464 [61] C. C. Allen, R. V. Morris, D. J. Lindstrom, M. M. Lindstrom, J. P.  
1465 Lockwood, Jsc mars-1: Martian regolith simulant, *Lunar and Planetary*  
1466 *Science* XXVIII (1997).
- 1467 [62] M. J. Wolff, M. D. Smith, R. T. Clancy, R. Arvidson, M. Kahre, F. See-  
1468 los IV, S. Murchie, H. Savijrvi, Wavelength dependence of dust aerosol  
1469 single scattering albedo as observed by the compact reconnaissance  
1470 imaging spectrometer, *Journal of Geophysical Research: Planets* 114  
1471 (2009).
- 1472 [63] W. Goetz, W. T. Pike, S. F. Hviid, M. B. Madsen, R. V. Morris, M. H.  
1473 Hecht, U. Staufer, K. Leer, H. Sykulka, E. Hemmig, J. Marshall, J. M.  
1474 Morookian, D. Parrat, S. Vijendran, B. J. Bos, M. R. El Maarry, H. U.  
1475 Keller, R. Kramm, W. J. Markiewicz, L. Drube, D. Blaney, R. E. Arvid-  
1476 son, J. F. Bell III, R. Reynolds, P. H. Smith, P. Woida, R. Woida, R. Tan-  
1477 ner, Microscopy analysis of soils at the phoenix landing site, mars: Clas-  
1478 sification of soil particles and description of their optical and magnetic  
1479 properties, *Journal of Geophysical Research: Planets* 115 (2010).
- 1480 [64] A. Pommerol, B. Jost, O. Poch, M. El-Maarry, B. Vuitel, N. Thomas,  
1481 The sciteas experiment: Optical characterizations of sublimating icy  
1482 planetary analogues, *Planetary and Space Science* 109110 (2015) 106 –  
1483 122.
- 1484 [65] R. Cerubini, A. Pommerol, Z. Yoldi, N. Thomas, Near-infrared re-  
1485 flectance spectroscopy of sublimating salty ice analogues. Implications  
1486 for icy moons, 211 (2022) 105391.

- 1487 [66] D. G. Blackburn, K. L. Bryson, V. F. Chevrier, L. A. Roe, K. F. White,  
1488 Sublimation kinetics of co2 ice on mars, *Planetary and Space Science*  
1489 58 (2010) 780–791.
- 1490 [67] R. N. Clark, P. G. Lucey, Spectral Properties of Ice Mineral Mixtures:  
1491 Implications on the Composition on the Galilean Satellites and Other Icy  
1492 Bodies., in: *Bulletin of the American Astronomical Society*, volume 13,  
1493 p. 700.
- 1494 [68] S.-M. Li, K.-S. Yang, C.-C. Wang, A semi-empirical model for predicting  
1495 frost properties, *Processes* 9 (2021).
- 1496 [69] Fornasier, S., Hasselmann, P. H., Barucci, M. A., Feller, C., Besse, S.,  
1497 Leyrat, C., Lara, L., Gutierrez, P. J., Oklay, N., Tubiana, C., Scholten,  
1498 F., Sierks, H., Barbieri, C., Lamy, P. L., Rodrigo, R., Koschny, D.,  
1499 Rickman, H., Keller, H. U., Agarwal, J., A´Hearn, M. F., Bertaux, J.-  
1500 L., Bertini, I., Cremonese, G., Da Deppo, V., Davidsson, B., Debei,  
1501 S., De Cecco, M., Fulle, M., Groussin, O., Güttler, C., Hviid, S. F.,  
1502 Ip, W., Jorda, L., Knollenberg, J., Kovacs, G., Kramm, R., Kührt, E.,  
1503 Küppers, M., La Forgia, F., Lazzarin, M., Lopez Moreno, J. J., Marzari,  
1504 F., Matz, K.-D., Michalik, H., Moreno, F., Mottola, S., Naletto, G., Pa-  
1505 jola, M., Pommerol, A., Preusker, F., Shi, X., Snodgrass, C., Thomas,  
1506 N., Vincent, J.-B., Spectrophotometric properties of the nucleus of  
1507 comet 67p/churyumov-gerasimenko from the osiris instrument onboard  
1508 the rosetta spacecraft, *A&A* 583 (2015) A30.
- 1509 [70] N. Thomas, G. Cremonese, R. Ziethe, M. Gerber, M. Brändli, G. Bruno,  
1510 M. Erismann, L. Gambicorti, T. Gerber, K. Ghose, M. Gruber,

1511 P. Gubler, H. Mischler, J. Jost, D. Piazza, A. Pommerol, M. Rieder,  
1512 V. Roloff, A. Servonet, W. Trottmann, T. Uthaicharoenpong, C. Zimmermann,  
1513 D. Vernani, M. Johnson, E. Pelò, T. Weigel, J. Viertl,  
1514 N. De Roux, P. Lochmatter, G. Sutter, A. Casciello, T. Hausner,  
1515 I. Fikai Veltroni, V. Da Deppo, P. Orleanski, W. Nowosielski, T. Zawistowski,  
1516 S. Szalai, B. Sodor, S. Tulyakov, G. Troznai, M. Banaskiewicz,  
1517 J. C. Bridges, S. Byrne, S. Debei, M. R. El-Maarry, E. Hauber,  
1518 C. J. Hansen, A. Ivanov, L. Keszthelyi, R. Kirk, R. Kuzmin, N. Mangold,  
1519 L. Marinangeli, W. J. Markiewicz, M. Massironi, A. S. McEwen,  
1520 C. Okubo, L. L. Tornabene, P. Wajer, J. J. Wray, The colour and stereo  
1521 surface imaging system (cassis) for the exomars trace gas orbiter, Space  
1522 Science Reviews 212 (2017) 1897–1944.

1523 [71] N. Thomas, G. Cremonese, R. Ziethe, M. Gerber, M. Brändli, G. Bruno,  
1524 M. Erismann, L. Gambicorti, T. Gerber, K. Ghose, M. Gruber,  
1525 P. Gubler, H. Mischler, J. Jost, D. Piazza, A. Pommerol, M. Rieder,  
1526 V. Roloff, A. Servonet, W. Trottmann, T. Uthaicharoenpong, C. Zimmermann,  
1527 D. Vernani, M. Johnson, E. Pelò, T. Weigel, J. Viertl,  
1528 N. De Roux, P. Lochmatter, G. Sutter, A. Casciello, T. Hausner,  
1529 I. Fikai Veltroni, V. Da Deppo, P. Orleanski, W. Nowosielski, T. Zawistowski,  
1530 S. Szalai, B. Sodor, S. Tulyakov, G. Troznai, M. Banaskiewicz,  
1531 J. C. Bridges, S. Byrne, S. Debei, M. R. El-Maarry, E. Hauber,  
1532 C. J. Hansen, A. Ivanov, L. Keszthelyi, R. Kirk, R. Kuzmin, N. Mangold,  
1533 L. Marinangeli, W. J. Markiewicz, M. Massironi, A. S. McEwen,  
1534 C. Okubo, L. L. Tornabene, P. Wajer, J. J. Wray, The colour and stereo  
1535 surface imaging system (cassis) for the exomars trace gas orbiter, Space

- 1536 Science Reviews 212 (2017) 1897–1944.
- 1537 [72] S. G. Warren, W. J. Wiscombe, J. F. Firestone, Spectral albedo and  
1538 emissivity of CO<sub>2</sub> in Martian polar caps: model results., 95 (1990)  
1539 14717–14741.
- 1540 [73] O. Poch, A. Pommerol, B. Jost, N. Carrasco, C. Szopa, N. Thomas,  
1541 Sublimation of water ice mixed with silicates and tholins: Evolution of  
1542 surface texture and reflectance spectra, with implications for comets,  
1543 Icarus 267 (2016) 154 – 173.
- 1544 [74] J. Eluszkiewicz, J.-L. Moncet, T. N. Titus, G. B. Hansen, A  
1545 microphysically-based approach to modeling emissivity and albedo of  
1546 the martian seasonal caps, Icarus 174 (2005) 524 – 534. Mars Polar  
1547 Science III.